A modular mRNA lipid nanoparticle platform rescues diverse genetic male infertility

Qi Kai Jiang[1#], Kexin Su[2#], Guangnan Li[1#], Huali Luo[3], Hao Wang[4], Jingwen Luo[1], Yukai Jason Zhong[1], Qiaodan Li[4], Zhihui Zhang[5], Haifeng Zhang[1], Wenlin Li[1], Banghua He[6], Chenyu Pei[1], Qin Li[1], Liang Xu Ma[1], Hongxiao Cui[1], Jiaoyan Ma[1], Deivendran Rengaraj[1], Linlin Zhang[6], Xianguang Yang[6], Zhefan Yuan[7], Lejun Li[8], Shuai Liu[2], and Xin Zhiguo Li[1*]

[1]Center for RNA Medicine, International Medical School, International Institutes of Medicine, The Fourth Affiliated Hospital, Zhejiang University School of Medicine, Yiwu, Zhejiang, 322000, China.

[2]College of Pharmaceutical Sciences, State Key Laboratory of Advanced Drug Delivery and Release Systems, Zhejiang University, Hangzhou, 310058, China.

[3]Department of Pathology, The Fourth Affiliated Hospital, Zhejiang University School of Medicine, International Medical School, International Institutes of Medicine, Zhejiang University, Yiwu, Zhejiang, 322000, China.

[4]Center for Reproductive Medicine, The Fourth Affiliated Hospital, Zhejiang University School of Medicine, International Medical School, International Institutes of Medicine, Zhejiang University, Yiwu, Zhejiang, 322000, China.

[5]Department of Laboratory Medicine, The Fourth Affiliated Hospital, Zhejiang University School of Medicine, International Medical School, International Institutes of Medicine, Zhejiang University, Yiwu, Zhejiang, 322000, China.

[6]College of Life Sciences, Henan Normal University, Xinxiang, Henan, 453002, China.

[7]CybernaX Biotechnologies, Hangzhou, Zhejiang, 311200, China.

[8]Department of Reproductive Endocrinology, Women's Hospital, Zhejiang University School of Medicine, Hangzhou, Zhejiang, 310006, China.

[#]These authors contributed equally to this work.

*Correspondence: XinLiRNA@zju.edu.cn(X.Z.L.)

Abstract

Genetic male infertility arises from diverse mutations that disrupt spermatogenesis, yet molecular therapies capable of restoring germ-cell function remain limited. Messenger RNA (mRNA) therapeutics offer transient protein replacement without permanent genome modification, but efficient and safe delivery to the seminiferous epithelium remains challenging. Here we develop a modular mRNA–lipid nanoparticle (LNP) platform that restores spermatogenesis across multiple genetic infertility models. Systematic comparison of clinically relevant ionizable lipids revealed that the clinically validated ionizable lipid MC3 uniquely provides sustained mRNA expression in the seminiferous epithelium while minimizing inflammation and systemic leakage. In contrast, lipids such as ALC-0315 produced higher transient reporter expression but failed to support functional rescue. A single intratesticular injection of an optimized *Papolb* mRNA restored spermiogenesis in ~25% of seminiferous tubules and generated functional sperm capable of producing healthy offspring through intracytoplasmic sperm injection. The platform extended to both meiotic (*Spo11*) and post-meiotic (*Btbd18*) arrest models and enabled efficient mRNA expression in cultured human seminiferous tubules. Comprehensive analyses demonstrated long-term safety in treated animals and multigenerational genetic and epigenetic stability in offspring. Together, these findings establish a modular mRNA–LNP platform for correcting diverse genetic causes of male infertility and reveal a design principle for extrahepatic RNA delivery: delivery efficiency alone does not predict functional therapeutic rescue, highlighting the importance of expression kinetics and tissue context in nanoparticle design.

Male infertility is a major public health problem with highly heterogeneous causes, affecting ~9% of reproductive-age men in the United States[1] and ~11% in China[2]. Nearly half of cases are idiopathic but thought to have a genetic basis, as spermatogenesis is regulated by more than 4,000 genes[3–5]. This complexity underscores the need for therapies that address specific genetic lesions rather than one-size-fits-all approaches. Assisted reproductive technologies (ART), such as in vitro fertilization (IVF) or intracytoplasmic sperm injection (ICSI), enable some men to father children but fail in more than half of treatment cycles[6] and remain inapplicable in the absence of viable sperm. About one third of couples never achieve a live birth despite repeated attempts[7]. For these patients, options are limited to donor gametes or childlessness, highlighting the urgent need for molecular therapies that restore endogenous spermatogenesis.

Messenger RNA (mRNA) therapeutics offer a programmable and transient means to restore protein expression without altering the genome. Spermatogenesis is highly dynamic—each human seminiferous cycle restarts every 72 days[8] and hundreds of seminiferous tubules generate tens of millions of sperm daily[9]—so the transient nature of mRNA aligns with the temporal demands of spermatogenic development. Even a brief restoration of a missing protein could generate enough functional sperm for assisted reproduction. Unlike DNA-based gene therapies, which raise ethical and safety concerns in germ cells[10], mRNA acts in the cytoplasm, and is not inherited. Unlike small molecule drugs, mRNA medicine can be flexibly reprogrammed for diverse genetic targets using the same delivery, design, and manufacturing platform. Furthermore, the clinical window is flexible because there is no immediate life-threatening urgency; treatment outcomes are easily monitored via semen analysis, and recovered sperm can be cryopreserved.

However, applying mRNA therapy to germ cells poses unique challenges. The testes are immune-privileged and protected by the blood–testis barrier (BTB), which restricts drug penetration and shields developing germ cells[11,12]. Moreover, meiotic and post-meiotic germ cells store large pools of untranslated mRNAs under tight temporal control[13].

Exogenous mRNAs may therefore fail to be translated or may be rapidly degraded. Safety is another paramount concern, as sperm RNAs carry epigenetic information that influences offspring development[14,15], and rare events of reverse transcription and genomic integration have been described[16]. Together, these hurdles have kept testicular mRNA therapy largely unexplored.

Previous studies have explored mRNA delivery to restore spermatogenesis in mouse models. In some cases, expression of exogenous mRNA restored histological features of spermatogenesis but did not yield functional sperm capable of producing offspring. These findings highlight that restoring germ-cell differentiation markers does not necessarily translate into functional fertility, underscoring the need to understand which delivery parameters determine biological rescue[17,18]. Two recent studies have demonstrated proof-of-concept testicular mRNA replacement in mouse models of genetic infertility. Mashiko et al. restored spermatogenesis in a meiotic-defect model using lipid nanoparticle–mediated delivery of *Pdha2* mRNA and produced offspring via ICSI[19]. Zhang et al. identified a spermatocyte-tropic lipid formulation through screening of custom ionizable lipids and achieved rescue across two meiotic-arrest models[20]. These advances establish the feasibility of intratesticular mRNA therapy. However, both approaches rely on newly developed or proprietary lipid formulations whose clinical scalability and translational readiness remain to be established, and safety evaluation has largely focused on short-term histology and limited genomic assessment. Rescue has been demonstrated primarily in meiotic-arrest contexts, leaving unresolved whether a unified delivery and RNA-design strategy can extend across genetically and developmentally distinct arrest stages, including post-meiotic spermiogenic defects. Moreover, efficient and compartment-restricted mRNA delivery in human seminiferous epithelium has not been directly evaluated, and cross-species feasibility remains a critical translational step. Finally, therapeutic success has often been interpreted in relation to peak delivery efficiency, without establishing whether maximal reporter expression necessarily predicts functional rescue within the highly structured seminiferous epithelium.

Here, we systematically optimize and validate a modular mRNA–LNP platform using clinically mature ionizable lipids, including DLin-MC3-DMA (MC3; used in the siRNA therapeutic patisiran), ALC-0315, and SM-102 (used in approved mRNA vaccines). Through head-to-head comparison in the testicular microenvironment, we identify context-dependent differences in biodistribution, retention, and immunogenicity that challenge the assumption that newer lipids are universally superior. We demonstrate that restoration of spermiogenesis in a *Papolb*-deficient model is associated with sustained expression duration rather than peak transfection efficiency. We further establish a reproduction-grade safety framework encompassing long-term structural integrity, somatic endocrine function, sperm functional competence, embryo transcriptomics, imprinting stability, and whole-genome sequencing–based integration analysis across generations. Finally, we show that the optimized platform extends across distinct arrest stages and enables efficient mRNA delivery in human seminiferous tissue ex vivo. Together, these findings define a context-dependent principle for extrahepatic mRNA therapeutics and provide a clinically informed, safety-evaluated framework for genetic forms of male infertility.

Results

Context-dependent optimization of mRNA delivery to the seminiferous epithelium

Delivering genetic material into the immune-privileged testis is challenging owing to the BTB and the specialized architecture of seminiferous tubules. We first compared four non-viral approaches—direct electroporation, protamine-mediated transfection, red blood cell membrane (RBCM) vesicle encapsulation, and lipid nanoparticles (LNPs)—for delivering mRNA to adult mouse testes. Despite protamine's ability to form cationic nanocomplexes with mRNA[21] and previous use of intratesticular electroporation to introduce DNA[22,23], none of the combinations tested (naked mRNA, protamine-condensed mRNA, electroporation, RBCM vesicle encapsulation, or combinations thereof) yielded more than background-level luminescence in the testis. Only the fully

combined method (mRNA + RBCM + electroporation) produced a detectable but weak luciferase signal, indicating limited tissue penetration and inefficient cytosolic release (Supplementary Fig. 1a, b).

In contrast, LNPs—vehicles widely used for nucleic acid delivery in vaccines and therapeutics—showed markedly superior delivery efficacy in the testis (Fig. 1a). To determine the optimal route for accessing germ-cell–containing compartments, we compared interstitial versus intratubular administration. Interstitial injection deposits nanoparticles into the testicular interstitium, primarily exposing Leydig and peritubular myoid cells, whereas infusion via the efferent duct (accessing the rete testis) fills seminiferous tubules and directly exposes the seminiferous epithelium, including germ cells and Sertoli cells. Intratubular infusion yielded 2.3–6.1-fold higher luciferase activity than interstitial injection at equivalent doses at 6–24 h post injection ($p < 0.01$; Fig. 1a). The procedure was well tolerated and required substantially lower doses than systemic administration. We therefore adopted intratubular delivery for all subsequent experiments.

To define which LNP formulation was most suitable for this tissue context, we formulated three clinically validated ionizable lipids—DLin-MC3-DMA (MC3), ALC-0315, and SM-102—with helper lipids (DSPC, cholesterol, PEG lipid). All yielded ~100–106 nm particles with low polydispersity and near-neutral ζ potentials (–6 to –3 mV; Supplementary Fig. 1c). Encapsulation efficiencies for luciferase mRNA were 94–98% (Supplementary Fig. 1c), and transmission electron microscopy confirmed comparable morphology across lipid types (Supplementary Fig. 1d), enabling a rigorous head-to-head comparison.

Following intratubular injection, SM-102 and ALC-0315 mediated higher peak luciferase signals in the testis than MC3, with SM-102 peaking at 6 h and MC3 and ALC-0315 peaking later (Fig. 1b). However, SM-102 consistently produced prominent off-target signal in the liver and spleen despite local administration (Fig. 1b, Supplementary Fig.

1e). This context-dependent leakage persisted even at a 75% lower dose (Supplementary Fig. 1f), indicating intrinsic differences in biodistribution and retention. Similar hepatic access of SM-102 has been reported following intramuscular vaccine administration[24]. Notably, MC3—optimized for hepatic siRNA delivery (e.g., Onpattro)[25] —did not exhibit comparable systemic leakage under local testicular delivery conditions. These findings indicate that LNP biodistribution is highly tissue-context dependent rather than determined solely by lipid generation or clinical precedent.

Innate immune activation further distinguished the formulations. At 12 h post injection, SM-102 induced substantial upregulation of *Tnf-α*, *Cxcl10*, *Il-6*, *Ifnb1*, and *Il-1β*, comparable to lipopolysaccharide controls (Fig. 1c), and was associated with visible testicular erythema (Supplementary Fig. 1g). Histological analysis revealed interstitial edema and leukocyte infiltration in SM-102–treated testes (Fig. 1d). Consistent with the observed off-target luciferase signal, SM-102 delivery was also associated with inflammatory changes in the liver. In contrast, MC3- and ALC-0315–treated testes showed only mild cytokine induction and minimal histological inflammation, with no detectable abnormalities in other organs (Supplementary Fig. 1h). Thus, despite similar particle size and morphology, ionizable lipid composition critically influenced tissue retention, systemic leakage, and immunogenicity within the seminiferous environment.

To define the cellular distribution of transfection, we delivered Cre mRNA formulated in MC3, ALC-0315, or SM-102 LNPs into Ai9 reporter mice (Rosa26 LoxP STOP LoxP tdTomato). Robust tdTomato expression was confined to the injected testis for MC3 and ALC-0315, whereas SM-102 again generated off-target liver and spleen signals (Supplementary Fig. 1i–j). Flow cytometric analysis of dissociated testicular cells demonstrated that >90% of distinct haploid (1n), diploid (2n), and tetraploid (4n) germ-cell populations were tdTomato^{+} following MC3 or ALC-0315 delivery (Fig. 1e; Supplementary Fig. 1m, n), indicating efficient transfection across spermatogenic stages. Immunostaining confirmed tdTomato co-localization with DDX4, a pan-germ-cell

marker expressed from spermatogonia through round spermatids (Fig. 1f), and with SOX9-positive Sertoli cells (Supplementary Fig. 1o), demonstrating seminiferous epithelial rather than germ-cell–exclusive targeting. Collectively, these findings establish efficient and broad transfection within the seminiferous epithelium.

Finally, we evaluated RNA format and modification chemistry to define an optimal expression profile. MC3 LNP–delivered N^1-methylpseudouridine–modified linear mRNA produced the highest peak GFP expression within three days, whereas self-amplifying mRNA (saRNA) and circular RNA (circRNA) yielded lower peak levels and elicited elevated innate immune responses at 24 hours yet sustained only low-level expression through day 14 (Supplementary Fig. 1p-r). Because sperm RNAs are known to transmit epigenetic information to offspring[14,15], prolonged RNA expression in germ cells could pose theoretical risks. We therefore prioritized linear modified mRNA, which provides transient yet robust expression. Compared with unmodified mRNA, N^1-methylpseudouridine-modified mRNA exhibited greater stability and markedly reduced cytokine induction in the immune-privileged testis[26,27] (Supplementary Fig. 1s-v). Collectively, these data establish that intratubular delivery of N^1-methylpseudouridine–modified mRNA formulated in MC3 LNP achieves efficient seminiferous epithelium transfection with minimal systemic leakage and limited innate immune activation. This optimized platform was therefore selected for therapeutic rescue experiments.

Sustained MC3-mediated expression in the seminiferous epithelium

We selected *Papolb* (also known as *Tpap*) as a model genetic infertility target because it encodes the testis-specific cytoplasmic poly(A) polymerase PAPOLB. Male *Papolb* mutants exhibit spermatogenic arrest at the round spermatid stage accompanied by increased germ-cell apoptosis and are infertile[28]. Quantification of seminiferous tubule stages in *Papolb* mutant testes indicated that approximately 30% of tubules contained round spermatids at seminiferous epithelial stages VII as reported[29], whereas the remaining tubules were distributed across earlier stages and no tubules progressed

beyond this arrest point. To restore PAPOLB function, we engineered an optimized *Papolb* mRNA with endogenous 5´UTR, codon-optimized coding region, and a heterologous stabilizing human α-globin 3´UTR (Fig. 2a). A small HA epitope tag was included for detection, which has previously been shown not to impair PAPOLB function[30]. RNA quality control confirmed integrity, minimal double-stranded RNA contamination (≤0.005%), and low endotoxin levels (< 4 EU mL^{-1}; Supplementary Fig. 2a,b).

Following intratubular delivery in wild-type mice, both MC3 and ALC-0315 LNPs produced HA–PAPOLB protein in the germ-cell cytosol within 10 h at the expected molecular weight (Fig. 2b,c). HA–PAPOLB expression was restricted to the injected testis and was undetectable in other organs (Supplementary Fig. 2c). Testis and epididymis morphology remained normal (Supplementary Fig. 2d), indicating that exogenous PAPOLB expression does not perturb spermatogenesis under optimized conditions.

We next compared expression kinetics between the two formulations. Although both MC3 and ALC-0315 mediated early HA–PAPOLB expression, their persistence differed markedly. By immunofluorescence, MC3-delivered protein remained detectable for approximately 10 days, whereas ALC-0315-delivered protein declined to near background by ~3 days. Western blot analysis showed a similar pattern, with detectable protein persisting to ~4 days for MC3 and ~2 days for ALC-0315 (Fig. 2b,c). Importantly, RT–qPCR analysis demonstrated that MC3-delivered *Papolb* mRNA remained detectable at low levels for up to ~14 days post injection, whereas ALC-0315-delivered transcript dropped below detection by ~5 days (Fig. 2d). While transcript persistence exceeded detectable protein levels—reflecting normal protein turnover and method-specific detection thresholds—all three assays consistently indicate that MC3 provides prolonged expression relative to ALC-0315. These data demonstrate that

expression duration differs substantially between lipid formulations within the seminiferous epithelium.

MC3-mediated *Papolb* mRNA restores spermiogenesis

We next administered a single intratubular injection of *Papolb* mRNA–LNP (without the HA tag) to *Papolb* knockout males. By day 7, MC3 LNP restored spermatid differentiation, evidenced by the appearance of elongating spermatids in multiple seminiferous tubules (Fig. 3a). Restoration of post-meiotic progression was confirmed using stage-specific markers. Protamine-1 and transition protein 1 (TNP1) staining demonstrated appropriate nuclear condensation during elongation (Fig. 3b; Supplementary Fig. 3a), and acrosome formation was confirmed by peanut agglutinin (PNA) staining (Fig. 3b). ACRV1 (SP-10), an acrosomal vesicle protein, exhibited the expected morphological transition from rounded signal in arrested round spermatids to elongated configuration following rescue (Supplementary Fig. 3b), consistent with acrosome remodeling.

Markers of earlier spermatogenic stages remained preserved. SYCP1, SYCP3, and γH2AX distributions were comparable between treated and control testes, indicating intact meiotic initiation and synapsis (Supplementary Fig. 3b,c). Spermatogonial proliferation (PCNA) and total histone H3 staining showed no gross alteration in early germ-cell populations or global chromatin organization (Supplementary Fig. 3d). Together, these findings indicate that rescue selectively restores post-meiotic differentiation without perturbing earlier spermatogenic stages.

Dose–response studies revealed that 0.4 mg mL^{-1} (~8 μg per testis) MC3– *Papolb* mRNA maximally rescued ~25% of tubules (Fig. 3c,d). This rescue was validated by Protamine-1 and PNA staining (Supplementary Fig. 3e), and improvement was further quantified by epithelial height, Johnsen scores and testis weight as well as decreased apoptosis relative to untreated *Papolb* mutants (Fig. 3d, Supplementary Fig. 3f). Lower

doses produced weaker rescue, whereas higher doses did not further improve spermatogenic recovery and instead increased inflammatory responses and apoptosis (Fig. 3c,d, Supplementary Fig. 3g), consistent with dose-dependent toxicity. These results indicate a defined therapeutic window in which sufficient mRNA expression restores spermiogenesis while higher doses introduce tissue stress that counteracts rescue.

Temporal analysis showed that elongating spermatids appeared by day 7, peaked at days 9–13 and declined by day 15; by day 17 tubules reverted to the arrest phenotype (Fig. 3e). Epithelial height and Johnsen scores as well as Protamine-1 and PNA staining mirrored this transient wave (Supplementary Fig. 3h,i). The transient effect matches the seminiferous epithelial cycle (~207 h, Supplementary Fig. 3j)[31], indicating that mRNA-rescued tubules undergo normal spermatogenesis. Multiple dosing, while extending the duration of sperm production, did not increase the percentage of rescued tubules (Supplementary Fig. 3k), suggesting a single injection is already sufficient to "jump-start" one cohort of spermatids.

In contrast, ALC-0315–formulated *Papolb* mRNA failed to rescue spermiogenesis at any examined time point (Fig. 3a; Supplementary Fig. 3l). Notably, the formulation that provided prolonged expression in Section 2 (MC3) was the only lipid capable of restoring spermatogenesis, whereas ALC-0315, despite higher peak reporter expression, did not yield functional rescue. Together with the expression kinetics data, these findings support an association between sustained expression duration and therapeutic rescue.

Rescued *Papolb* sperm support embryo development and germline transmission

To determine whether restored spermiogenesis yielded functionally competent gametes, we analyzed sperm recovered from MC3-treated *Papolb*-deficient testes (Fig. 4a). Testicular sperm exhibited normal head–tail morphology by Diff-Quik staining, comparable to heterozygous *Papolb*$^{+/-}$ littermate controls (Fig. 4b). Mitochondrial membrane potential was assessed using membrane potential-dependent Mitotracker,

TMRE, and JC-1 assays with carbonyl cyanide m-chlorophenyl hydrazone (CCCP) as a depolarization control (Fig. 4c; Supplementary Fig. 4a,b). Rescued sperm displayed preserved mitochondrial polarization patterns similar to controls. DNA integrity, evaluated by Comet assay, showed no increase in fragmentation relative to heterozygous testicular sperm (Fig. 4d). Together, these analyses indicate that rescued sperm are structurally intact and bioenergetically competent.

Because intratubular infusion disrupts normal sperm transit to the epididymis (Supplementary Fig. 4c–e), reproductive competence was evaluated using ICSI with testicular sperm. Testicular sperm from MC3-treated *Papolb*$^{-/-}$ males fertilized wild-type oocytes at rates comparable to heterozygous controls. Approximately 79% of injected metaphase II oocytes progressed to the two-cell stage, similar to heterozygous testicular sperm (~83%) and modestly lower than epididymal sperm (~97%) (Fig. 4e,f). Transfer of two-cell embryos into pseudopregnant females yielded live F1 offspring at ~20% per transferred embryo. When maintained in vitro, embryos progressed through subsequent cleavage stages, and representative blastocysts were observed (Supplementary Fig. 4f).

F1 offspring (designated "Papi") exhibited normal postnatal growth trajectories and litter sizes (Fig. 4g; Supplementary Fig. 4g), with no overt morphological abnormalities. Sex ratios of offspring were comparable across groups, including *Papolb*$^{+/-}$ epididymal sperm (male 54.8%, female 45.2%), *Papolb*$^{+/-}$ testicular sperm (male 57.6%, female 42.4%), and Papi F1 offspring (male 55.2%, female 44.8%), consistent with no detectable sex-biased developmental impact. Comprehensive phenotypic assessment revealed no detectable differences in gross organ morphology, body composition (lean mass, fat mass, and bone density), or hematological and serum biochemistry parameters compared with controls (Supplementary Fig. 4h–l). Behavioral assays, including open field and object recognition tests, showed no detectable alterations in locomotor activity, anxiety-like behavior, or cognitive performance (Fig. 4h, Supplementary Fig. 4m). Sexual

behavior parameters—including mounting latency, intromission latency, and copulatory duration—were comparable to heterozygous controls (Supplementary Table 1).

Importantly, Papi males were fertile and produced normal number of F2 pups per litter and via natural mating (Fig. 4i), and F2 animals displayed normal growth patterns (Fig. 4g, Supplementary Fig. 4n). Fertility was maintained into the F3 generation (Supplementary Fig. 4o), indicating stable germline transmission across multiple generations. All offspring derived from treated sires were heterozygous carriers, consistent with transient mRNA supplementation rather than genomic modification (Supplementary Fig. 4p).

To assess endocrine consequences of germline rescue, serum testosterone, FSH, and LH levels were measured. As expected, untreated *Papolb* mutants exhibited reduced testosterone and compensatory elevation of gonadotropins (Fig. 4j). These findings are consistent with the concept that germ-cell–specific defects can be functionally bypassed without directly correcting endocrine feedback mechanisms[32,33]. Although spermiogenesis was restored following MC3-mediated *Papolb* delivery, systemic hormone levels were not fully normalized at early time points, consistent with rescue restricted to the germ-cell compartment rather than correction of hypothalamic–pituitary–gonadal axis signaling. Hormone levels in F1 and F2 progeny fell within normal physiological ranges (Supplementary Fig. 4q), indicating preserved endocrine homeostasis across generations.

Collectively, these results demonstrate that MC3-mediated *Papolb* mRNA delivery restores spermiogenesis to a level sufficient for ICSI competence and supports normal development, reproductive behavior, and stable germline transmission without overt physiological abnormalities.

Long-term safety in treated F0 males

Given the translational implications of germline-directed mRNA delivery, we evaluated long-term safety in treated F0 *Papolb*-deficient males following optimized intratubular MC3-mediated mRNA administration. We first assessed inflammatory responses. Immunofluorescence analysis of the macrophage marker F4/80 revealed no increase in macrophage infiltration at either early (11 days) or late (6 months) time points compared with heterozygous controls (Fig. 5a), indicating absence of persistent inflammatory activation. Because sustained inflammation can lead to tissue remodeling and fibrosis, we next examined collagen deposition by Masson's trichrome staining. No abnormal interstitial collagen accumulation was observed in treated testes relative to controls, whereas skin served as a positive control for collagen detection (Fig. 5b), indicating absence of fibrotic remodeling. Histological examination by hematoxylin and eosin staining further demonstrated preserved seminiferous architecture without tubular atrophy, interstitial thickening, or chronic inflammatory infiltrates (Supplementary Fig. 5a). Together, these findings indicate maintenance of structural integrity in treated testes.

We next evaluated functional integrity of somatic compartments. Because Sertoli cells maintain the BTB, Claudin11 immunostaining was performed. Claudin11 exhibited a continuous linear distribution along the basal compartment of seminiferous tubules in treated and control testes, with no evidence of junctional disruption (Fig. 5c), indicating preserved BTB integrity. Leydig cell steroidogenic function was assessed by CYP17A1 expression. Immunofluorescence and quantitative western analysis showed comparable localization and expression levels between treated and control testes (Fig. 5d,e), suggesting intact endocrine support within the testis.

Finally, systemic safety was evaluated. No evidence of acute toxicity was observed in major organs between day 1 and day 21 following MC3-mediated *Papolb* mRNA delivery in either control or mutant mice (Supplementary Fig. 5b,c). Histological examination of heart, liver, spleen, lung, kidney, and brain at 6 months similarly revealed no structural abnormalities or inflammatory changes (Supplementary Fig. 5a), indicating

absence of long-term organ pathology. Consistent with no morphological changes, serum biochemistry parameters—including liver enzymes (ALT, AST), renal function markers (BUN, creatinine), glucose, and LDH—remained within normal ranges across time points (Fig. 5f; Supplementary Fig. 5d). Transient hematological fluctuations observed shortly after injection resolved during follow-up and remained stable thereafter (Fig. 5f; Supplementary Fig. 5e), consistent with short-term procedural stress rather than sustained systemic toxicity.

Collectively, these findings demonstrate that optimized intratubular delivery of modified mRNA formulated in MC3 LNP does not induce chronic inflammation, fibrosis, barrier disruption, somatic dysfunction, or systemic toxicity in treated F0 males.

Multigenerational genetic and epigenetic integrity following *Papolb* rescue

To assess imprinting stability, we performed targeted methylation analysis of canonical differentially methylated regions (DMRs), including *H19*, *Peg3*, and *Snrpn*. Pyrosequencing across multiple CpG sites revealed no significant differences in mean methylation levels between offspring derived from treated sires and heterozygous controls (Fig. 6a, Supplementary Fig. 6a). Analysis at individual CpG positions similarly showed no significant differences after correction for multiple comparisons. Overall methylation patterns were highly concordant across groups, consistent with preserved imprinting within detection limits.

Because early embryogenesis is particularly sensitive to epigenetic perturbation, we analyzed transcriptomes of late two-cell and four-cell embryos generated via ICSI using sperm from treated males. Transcriptomic profiles between embryos derived from treated and control males were highly correlated at both developmental stages (Fig. 6b). Differential expression analysis identified only a limited subset of genes with FDR < 0.05. Notably, transcriptomic concordance increased at the four-cell stage ($r = 0.73$, $P < 2.2 \times 10^{-16}$, $\rho = 0.72$, $P < 2.2 \times 10^{-16}$) compared with the two-cell stage ($r = 0.64$, $P < 2.2$

x 10^{-16}, ρ= 0.62, $P < 2.2 \times 10^{-16}$), consistent with the higher stochastic variability associated with the earliest phase of zygotic genome activation and the stabilization of transcriptional programs thereafter.

To evaluate potential genomic integration of delivered *Papolb* mRNA, we performed whole-genome sequencing at approximately 30× coverage on F0 treated testes (n = 3), F0 treated liver (n = 3), and F1 testes (n = 3), together with an untreated control. Reads were aligned to an augmented reference genome incorporating the exact *Papolb* cDNA sequence as an additional contig. Structural variant analysis integrating split-read and discordant read-pair evidence identified no high-confidence breakend events linking genomic loci to the transgene contig (Fig. 6c). In parallel, genome-wide copy-number variation (CNV) analysis was performed using 1 Mb genomic bins. Across all F0 and F1 samples, log2 fold-change profiles remained centered around zero with no evidence of chromosome-scale or focal copy-number alterations exceeding 1 Mb (Supplementary Fig. 6c), indicating absence of detectable large-scale genomic rearrangements.

At this sequencing depth, heterozygous germline insertions (~50% allele fraction) would be expected to generate ~15 independent supporting reads and are therefore robustly detectable under our filtering criteria (minimum ≥3–5 supporting fragments). Insertions present at ≥10% allele fraction would likewise yield multiple supporting split or discordant reads and fall within the sensitivity range of our analysis. Although extremely rare mosaic events below this threshold cannot be formally excluded, no integration-supporting reads were observed in any F0 or F1 sample. To further define analytical sensitivity, serial dilution of *Papolb* cDNA was used to establish PCR detection limits (10^{-5}–10^{-7} depending on primer set). Using equivalent genomic DNA input from F1 mice, no amplification consistent with reverse-transcribed *Papolb* mRNA integration was detected (Fig. 6d).

Collectively, these data demonstrate that MC3-mediated intratubular delivery of modified *Papolb* mRNA does not result in detectable genomic integration, large-scale structural

variation, imprinting disruption, or early embryonic transcriptional abnormalities within the limits of detection.

Extension of the modular platform to additional infertility models and human tissue

To assess broader applicability, we applied the optimized MC3-formulated mRNA strategy (Fig. 2a) — incorporating codon optimization, retention of the endogenous 5′UTR, and a stabilizing human α-globin 3′UTR — to two additional genetic models of male infertility representing distinct etiologies and developmental arrest stages. *Spo11* is required for programmed meiotic double-strand break formation at the leptotene stage; its deficiency results in early meiotic arrest due to failure of homologous synapsis[34,35]. In contrast, *Btbd18* regulates transcription of a subset of pachytene piRNA precursors, and its deficiency leads to post-meiotic arrest at the round spermatid stage[36]. These models therefore represent mechanistically distinct defects spanning meiosis and spermiogenesis.

In *Spo11* mutants, intratubular delivery of *Spo11* mRNA restored meiotic progression, as demonstrated by chromosome spread analysis (Fig. 7a). Whereas untreated mutants arrested at early zygotene without progression to pachytene, treated testes exhibited restored pachytene and diplotene cells, indicating recovery of homologous synapsis. Consistent with the earlier developmental arrest in this model, elongating spermatids emerged later than in *Papolb* mutants, appearing between days 19–25 post-injection (Fig. 7b). In *Btbd18*-deficient mice, elongating spermatids were detected between days 17–23 following treatment (Fig. 7b). Immunostaining for PNA, Protamine-1, and TNP1 confirmed restoration of late-stage spermiogenesis in both models, while PCNA and γH2AX staining indicated preserved early germ-cell proliferation and meiotic chromatin organization (Supplementary Fig. 7a–c).

Quantitative analysis revealed that approximately 19.6% of seminiferous tubules in *Spo11* mutants and 12.9% in *Btbd18* mutants exhibited restored spermatogenesis at peak time points, whereas PBS-treated controls showed no rescue (Fig. 7c). As in the *Papolb*

model, mature sperm accumulation in the epididymis was not observed (Supplementary Fig. 7d), consistent with disruption of sperm transit caused by the surgical procedure.

Testicular sperm collected from treated *Spo11* and *Btbd18* males exhibited normal morphology (Supplementary Fig. 7e) and supported embryo development via ICSI, yielding two-cell embryos at rates comparable to heterozygous controls (Fig. 7d; Supplementary Fig. 7f). Viable F1 offspring were generated. Sex ratios of ICSI-derived F1 offspring were near expected values in both models (*Spo11* mutants: male 58.1%, female 41.9%; *Spo11*$^{+/-}$ testicular sperm control: male 53.3%, female 46.7%; *Btbd18* mutant: male 52.8%, female 47.2%; *Btbd18*$^{+/-}$ testicular sperm control: male 48.5%, female 51.5%). F1 exhibited normal postnatal growth (Fig. 7e; Supplementary Fig. 7g), and genotyping confirmed expected Mendelian inheritance patterns (Supplementary Fig. 7h).

To evaluate translational feasibility, we established short-term culture of mouse and human seminiferous tubules in parallel (Supplementary Fig. 7i,j). A total of 13 independent human donor samples were used to optimize the culture and delivery conditions, and three randomly selected donors were analyzed in detail with parallel replicates. No marked inter-individual variability in delivery efficiency was observed. Following intratubular microinjection, luciferase expression was detected within germ-cell–containing compartments at 24 h in both mouse and human tubules, with reduced but detectable signal at 48 h (Fig. 7f; Supplementary Fig. 7k). HA-tagged protein expression co-localized with RNF17-positive germ cells in both species, whereas negative controls lacked detectable signal (Fig. 7g; Supplementary Fig. 7l). These results demonstrate that the optimized mRNA–LNP platform can transfect human seminiferous tissue under controlled ex vivo conditions.

Together, these findings indicate that the modular mRNA–LNP strategy extends across distinct genetic etiologies and developmental arrest stages and is compatible with human seminiferous epithelium.

Discussion

Our study establishes a modular mRNA–lipid nanoparticle (LNP) platform capable of restoring spermatogenesis and functional fertility across multiple genetic models of male infertility without genomic modification. Building upon recent demonstrations that intratesticular mRNA delivery can rescue spermatogenesis in individual mouse models[19,20], our work provides a systematic nanotechnological optimization and broader biological validation of this therapeutic concept. By directly comparing clinically relevant LNP formulations in the seminiferous environment, we identify the FDA-approved ionizable lipid MC3 as uniquely capable of achieving sustained mRNA expression within germ cells while minimizing inflammation and systemic leakage. A single intratesticular injection of optimized *Papolb* mRNA restored spermiogenesis in approximately one quarter of seminiferous tubules, generating functional sperm that produced healthy offspring through ICSI and supported normal multigenerational development. Importantly, the platform proved modular: similar strategies restored spermatogenesis in both meiotic (*Spo11*) and post-meiotic (*Btbd18*) arrest models and enabled efficient mRNA delivery to cultured human seminiferous tubules. Together, these results establish a broadly applicable and clinically informed framework for mRNA-based treatment of genetic male infertility.

The biological behavior of rescued testes provides insight into the limits of spermatogenic recovery. Although MC3-mediated *Papolb* delivery restored spermiogenesis in a subset of seminiferous tubules, the proportion of rescued tubules did not increase with repeated dosing. Histological analysis indicated that approximately 25% of tubules in *Papolb* mutant testes contained germ cells at the round spermatid stage, consistent with the developmental stage at which the mutation causes arrest. Because spermiogenesis from round spermatids to elongating spermatids typically requires approximately 10–14 days in the mouse testis[37], only those tubules containing germ cells within the appropriate developmental window at the time of treatment are

capable of completing a rescued differentiation wave. This interpretation is consistent with the expression kinetics of the lipid formulations: MC3-mediated delivery produced sustained expression for approximately two weeks, overlapping with the developmental window required for spermatid maturation, whereas ALC-0315 produced only short-lived expression. Together these observations suggest that therapeutic efficacy depends on the alignment between post-delivery expression kinetics and the intrinsic developmental timing of the seminiferous epithelium. Repeated intratubular injections did not substantially increase rescue efficiency, likely reflecting the asynchronous progression of seminiferous tubules through the epithelial cycle and the limited proportion of tubules that are responsive at any given time. Together, these observations indicate that successful rescue depends on whether post-delivery protein expression persists long enough to span the developmental window of spermiogenesis, linking nanoparticle expression kinetics directly to therapeutic outcome.

Translational considerations differ between mouse and human testes. In mice, intratubular delivery requires surgical exposure and efferent-duct infusion, which disrupts epididymal sperm transport and necessitates the use of testicular sperm for assisted reproduction. In humans, however, the scrotal position of the testes may permit minimally invasive ultrasound-guided intratesticular or rete-testis injection procedures that preserve epididymal transport. Under such conditions, rescued sperm could potentially enter the ejaculate, enabling reproductive options ranging from ICSI to conventional assisted reproduction and possibly natural conception if sufficient sperm production is restored. Although the present study focuses on monogenic infertility models, human infertility may be genetically complex; the modular nature of mRNA therapeutics raises the possibility that multiplexed mRNA delivery could eventually address more complex etiologies, although such approaches will require careful evaluation given the developmental sensitivity of the testis. Together with our demonstration of efficient mRNA expression in cultured human seminiferous tubules, these observations suggest that localized RNA delivery to human testes may be

technically feasible, although further optimization and safety evaluation in large-animal models will be required before clinical translation.

Given the germline-directed nature of this intervention, safety was a central focus of our study. We therefore established complementary safety frameworks examining both long-term effects in treated individuals (F0) and multigenerational outcomes in their descendants (F1–F3). Treated F0 males showed no evidence of chronic inflammation, fibrosis, BTB disruption, endocrine dysfunction, or systemic toxicity. Offspring generated from rescued sperm exhibited normal development, reproductive competence, and physiological function across multiple generations. At the molecular level, imprinting methylation patterns, early embryonic transcriptomes, and somatic tissue gene expression profiles were indistinguishable from controls. Whole-genome sequencing combined with structural-variant detection and PCR sensitivity analysis revealed no detectable genomic integration of *Papolb* mRNA. Together these findings indicate that transient mRNA-mediated protein replacement can restore germ-cell function without detectable long-term or heritable genomic perturbation within current detection limits.

Because this strategy restores fertility without altering genomic DNA, it raises distinct ethical considerations compared with germline genome editing. The mRNA therapy described here provides transient protein replacement and does not introduce permanent genetic modifications; offspring inherit parental alleles in their natural configuration. Some have expressed concern that restoring fertility in individuals carrying infertility-associated mutations could propagate these alleles in the population. However, many infertility genes exhibit pleiotropic biological roles and their evolutionary significance remains incompletely understood. In addition, implementation of such precision therapies will initially depend on accurate genetic diagnosis, which may currently be limited by access to sequencing technologies. As RNA therapeutics continue to expand into reproductive medicine, ongoing dialogue among scientists, clinicians and ethicists will be

important to ensure that emerging technologies are evaluated within appropriate scientific and societal contexts.

From a nanotechnology perspective, our results suggest that delivery efficiency alone is not a reliable predictor of functional therapeutic rescue in complex tissues. Lipids such as SM-102 and ALC-0315, which perform well in hepatic and intramuscular mRNA delivery[38,39], produced strong early reporter expression in the testis but also induced inflammation and systemic leakage that limited therapeutic efficacy. In contrast, MC3 exhibited slower release kinetics and prolonged retention in the seminiferous epithelium, producing sustained expression that overlapped with the developmental timing required for spermatid maturation. These findings indicate that successful RNA therapeutics may depend on matching nanoparticle expression kinetics to the biological therapeutic window of the target tissue, rather than maximizing peak delivery alone. Consistent with this concept, previous studies[17,18] reported restoration of spermatogenic morphology after mRNA delivery without recovery of functional fertility, demonstrating that the reappearance of differentiation markers does not necessarily translate into developmentally competent sperm. Together, these observations suggest that optimization of LNP systems for extrahepatic RNA therapeutics should prioritize functional rescue and temporal alignment with tissue biology rather than relying solely on reporter expression or short-term toxicity metrics.

Beyond its therapeutic potential, this platform may also provide a useful experimental tool for reproductive biology. Germ cells have historically been difficult to transfect, limiting functional interrogation of genes involved in spermatogenesis. Efficient delivery of mRNA or genome-editing components into the adult testis using clinically relevant LNP formulations could enable rapid in vivo functional studies, complementing traditional genetic models and expanding the experimental toolkit for studying germ-cell development.

In summary, we define a modular and clinically informed mRNA–LNP platform that restores spermatogenesis across multiple genetic etiologies while maintaining long-term and multigenerational safety. Our findings highlight the importance of context-dependent nanoparticle design for extrahepatic RNA delivery and demonstrate that expression persistence, tissue retention and functional rescue metrics should guide LNP optimization beyond conventional measures of peak transfection efficiency or acute toxicity. These insights provide both a foundation for developing molecular therapies for genetic male infertility and design principles for the development of LNP systems targeting other extrahepatic tissues.

Methods

Nanoparticle formulation and characterization

Formulation:
Lipid nanoparticle (LNP) formulations were prepared by a rapid ethanol dilution method, similar to published protocols[40]. Briefly, an ionizable lipid (such as ALC-0315, SM-102, or MC3; obtained from UTgene, Cat# UT1001, UT1002, UT1003, respectively) and helper lipids – cholesterol (Sigma–Aldrich, C8667), 1,2-distearoyl-sn-glycero-3-phosphocholine (DSPC; Avanti, 850365P), ALC-0159 (AVT (Shanghai) Pharmaceutical Tech, Cat# 002009), and a polyethylene glycol conjugated lipid (PEG-lipid; AVT, Cat# 002005) – were dissolved together in absolute ethanol at defined molar ratios. MC3 LNPs were formulated with DLin-MC3-DMA, DSPC, cholesterol and DMG-PEG2000 at a molar ratio of 50:10:38.5:1.5. For SM-102 LNPs, the molar ratio of SM-102/DSPC/cholesterol/DMG-PEG2000 was 50:10:38.5:1.5. ALC-0315 LNPs were formulated with ALC-0315/DSPC/cholesterol/ALC-0159 at a molar ratio of 46.3:9.4:42.7:1.6. The nucleic acid cargo (e.g., mRNA) was diluted in an acidic buffer (10 mM citrate, pH ~4.0). The ethanol lipid solution was rapidly mixed with the aqueous RNA solution at a fixed 1:3 volume ratio (organic : aqueous) to promote spontaneous self-assembly of nanoparticles. The mixture was incubated at room temperature for ~10

minutes to allow vesicle formation. For in vivo use, the crude LNP suspension was further purified by dialysis against PBS to remove residual ethanol and any unencapsulated RNA, then concentrated in PBS by ultrafiltration to the desired nucleic acid concentration. The specific ionizable lipid and type of nucleic acid cargo used in each experiment are detailed in the Results (and figure legends). In general, the nucleic acid cargos included various mRNA constructs, a self-amplifying mRNA (saRNA), or a circular RNA (circRNA). The sources of these constructs were as follows: *Papolb* mRNA and saRNA were synthesized in-house by in vitro transcription; Cre mRNA was purchased from RNAlfa Biotech (Cat# Alfa-2501); firefly luciferase mRNA was from Levostar (Cat# LS-RM021); and the circRNA was obtained from Novoprotein (Cat# MR201-U100).

Characterization:

The hydrodynamic diameter and polydispersity index (PDI) of LNPs were measured by dynamic light scattering (DLS) using a Malvern Zetasizer Nano instrument. Samples were diluted in PBS and equilibrated at room temperature before analysis. Size is reported as the intensity-weighted mean diameter, with PDI as a measure of dispersity.

The surface ζ-potential of the nanoparticles was determined on the same instrument using folded capillary cells, after diluting samples ~50-fold in deionized water.

Encapsulation efficiency of mRNA was assessed with a RiboGreen RNA fluorescence assay (Thermo Fisher Quant-iT™ RiboGreen kit), by treating aliquots of the LNP with or without 0.2% Triton X-100 to distinguish encapsulated vs. total RNA. Encapsulation efficiency (%) was calculated as 100 × (protected RNA / total RNA input).

Animal experiments

All animal procedures were performed in accordance with institutional and national guidelines for animal welfare and were approved by the Laboratory Animal Welfare and

Ethics Review Committee of Zhejiang University (ZJU20220156 and ZJU20250897). The protocol adhered to principles of humane care, and measures were taken to ensure animal well-being throughout the experiments. Housing conditions: temperature 20–26 °C, humidity 40–70%, 12 h light/dark cycle (lights on at 7:30; off at 19:30), normal chow diet, corn cob bedding, cage density of 5 mice per cage.

Mouse strains: Wild-type C57BL/6J mice (Jackson Laboratory, stock #000664) were used for most in vivo experiments. B6.Cg-*Gt(ROSA)26Sor*$^{tm9(CAG\text{-}tdTomato)Hze}$/J reporter mice (the Ai9 line; JAX stock #007909), *Papolb* knockout mice (*Papolb*$^{-/-}$) were obtained from RIKEN BioResource Center[28,41], *Spo11* knockout mice were constructed according to the previous publication[34], and *Btbd18* knockout strain[36] were maintained on a C57BL/6 background. Mice were genotyped by PCR on tail DNA (using primers provided by the source repository). To test the potential integration of *Papolb* mRNA, we used primers targeting the coding sequence of the delivered mRNA (which was codon-optimized, distinct from the genomic copy; primer sequences used for all genotyping were provided in Supplementary Table 1). Unless otherwise noted, experimental cohorts consisted of young adult male mice (aged over 6 weeks, average 25 g body weight) to ensure sexual maturity. Mice were randomly assigned to treatment groups, and investigators were blinded to group allocations during outcome assessments wherever possible (see Statistical analysis below). Number of animals per group: n = 3 for LNP delivery, rescue, and fertility; n = 5 for behavioral assays and sexual activity.

In vivo administration of nanoparticles / mRNA

Two delivery routes were used, depending on the target cell population: (1) injection via the rete testis/efferent duct to deliver material into the seminiferous tubules (targeting primarily Sertoli cells and germ cells), and (2) direct interstitial injection into the testis parenchyma (targeting Leydig cells and other interstitial cells). In each case, adult male mice were anesthetized with 2.5% tribromoethanol in PBS (Avertin, i.p., MeilunBio, MA0478) and placed supine on a sterile surgical platform. For the rete testis (tubular)

delivery, a small lower abdominal incision (~1 cm) was made to exteriorize the testis within the tunica. Using a dissecting microscope, the efferent ducts emerging from the testis (near the junction with the epididymis) were identified. A fine pulled-glass micropipette (tip diameter ~50–80 µm) pre-loaded with the RNA solution (with a trace of 0.05% Fast Green dye added for visibility) was carefully inserted into the lumen of the efferent duct. Approximately 20 µL of solution was slowly injected at 3–5 µL/sec; successful delivery into the seminiferous tubules was confirmed by observing the dye spreading from the rete testis throughout the tubules (visible as faint green coloration filling the testis) (Fig.1a). For interstitial injections, a 30-gauge needle (Hamilton syringe) was inserted directly into the testis parenchyma, and ~20 µL of solution was delivered into the interstitial space between tubules at the same rate. Care was taken to inject slowly and avoid excessive pressure to prevent tissue rupture or back-leakage. After either type of injection, the abdominal incision was closed with absorbable sutures. Analgesia: Ibuprofen (50–60 mg/kg/day; 10 mL of Children's Motrin in 500 mL of water) continuously in drinking water for 3 days post-surgery. Mice were monitored during recovery from anesthesia and returned to their home cages once fully ambulatory.

Dosing regimens

Doses of the nucleic acid cargo were selected based on preliminary studies and prior literature. Ai9 reporter mice received LNP-encapsulated Cre mRNA via tail vein injection at a dose of 10 µg mRNA per mouse (approximately 0.4 mg/kg body weight). For luciferase reporter studies, mice were administered firefly luciferase mRNA–LNP at 10 µg (0.4 mg/kg) (by intramuscular or intratesticular injection) as detailed in the Results section. *Papolb* knockout mice assigned to gene therapy received an i.t. dose of LNPs carrying *Papolb* mRNA at 0.32 mg/kg. In some experiments, self-amplifying mRNA (saRNA) or circular RNA (circRNA) formulations were administered via the same routes; the dosing for saRNA and circRNA (10 µg per testis, 0.4 mg/kg) was comparable to the mRNA doses. Control animals received equivalent volumes of vehicle (PBS). All

treatments were given as a single dose unless otherwise noted. No animals were excluded from analysis a priori except in the case of a technical failure (e.g., if an injection was visibly mis-delivered); in this study, no such exclusions were necessary. Body weights at dosing: 25 g. Dose-response experiments: *Papolb* KO mice received 2, 4, 8, or 16 µg *Papolb* mRNA–LNPs (n = 2 mice per dose). Samples were collected on day 7 post-injection. Time-course experiments: *Papolb* KO mice treated with 8 µg *Papolb* mRNA–MC3 LNPs were sampled at 7, 9, 11, 13, 15, 17, 19, and 21 days post-injection. *Btbd18* KO mice were sampled on day 13 and 19, and *Spo11* KO mice on day 15 and 21.

In vivo fluorescence and bioluminescence imaging

Fluorescence imaging (tdTomato reporter):
To evaluate nanoparticle biodistribution and transgene expression in vivo, mice were imaged using an IVIS Spectrum optical imaging system (BIOSPACE LAB Photon IMAGER Optima) at various time points after treatment. For the *Cre* mRNA delivery studies using Ai9 reporter mice, animals were euthanized, dissected and major organs (including testes, liver, spleen, kidneys, lungs, and heart) harvested for ex vivo fluorescence imaging at 48 hours post-injection. tdTomato fluorescence was captured using the appropriate excitation/emission filter settings (Ex 570 nm / Em 620 nm). Identical imaging parameters (illumination intensity, exposure time, binning, etc.) were used for all animals to allow quantitative comparison. Fluorescence intensity was quantified as radiant efficiency within regions of interest (ROIs) using M3Vision® software (BIOSPACE LAB).

Bioluminescence imaging (luciferase reporter):
For luciferase experiments, bioluminescence imaging was performed at designated timepoints. To compare different intratesticular injection routes (rete testis vs interstitial), images were collected at 6, 9, 12, and 24 h. To compare different LNP formulations (MC3, ALC-0315, SM-102) and assess SM-102 leakage, images were collected at 1, 3, 6, 9, 12, and 24 h post-injection. Mice were injected intraperitoneally with D-luciferin (150

mg/kg, 100 µL; Gold Biotechnology, LUCNA-100) and anesthetized with isoflurane 5 min later. Photons emitted from firefly luciferase activity were collected with a 5 s exposure, standard binning, and consistent field of view. Data were analyzed as total photon flux (photons/sec) within ROIs encompassing the testes or other relevant regions. Baseline auto-luminescence was negligible.

Tissue preparation and immunofluorescence microscopy

Frozen-section imaging of native tdTomato:
For high-resolution analysis, testes and other relevant organs were collected, embedded fresh in optimal cutting temperature (O.C.T.) compound, flash-frozen on dry ice, and stored at −80 °C until sectioning. Cryostat sections (5 µm) were mounted on glass slides, briefly fixed in 4% paraformaldehyde (PFA) or acetone, counterstained with DAPI, and mounted in antifade medium.

Immunofluorescence staining of testis sections:
Other testis samples were fixed in 4% PFA (overnight at 4 °C), dehydrated, cryoprotected in 30% sucrose, and sectioned at 5 µm. After washing in PBS, sections underwent heat-mediated antigen retrieval (10 min in citrate buffer pH 6.0). Blocking was performed in 5% normal goat serum with 0.1% Triton X-100 for 1 h. Primary antibodies were incubated overnight at 4 °C: SOX9 (HuaBio, Cat# ET1611-56, 1:500), PRM1 (Briar Patch, Hup-1N, 1:200), and HA-tag (CST, clone C29F4, 1:500). Alexa Fluor 488–conjugated peanut agglutinin (PNA, Thermo Fisher L21409; 2 µg/mL) was used for acrosomes. After PBS washes, slides were incubated for 1 h with Alexa Fluor 488 goat anti-rabbit (Invitrogen A-11008, 1:500) and Alexa Fluor 594 goat anti-mouse (Invitrogen A-11005, 1:500). Nuclei were counterstained with DAPI. Imaging was performed on a Zeiss Axio Imager.M2 microscope with fixed acquisition settings across groups.

Histological analysis

For general assessment of morphology and toxicity, testes were fixed in Bouin's solution overnight at 4 °C, transferred to 70% ethanol, dehydrated, and paraffin embedded. Sections (3 µm) were stained with hematoxylin and eosin (H&E) using standard protocols. Slides were examined by a blinded observer. Features evaluated included seminiferous tubule structure, presence or absence of elongating/elongated spermatids, epithelial height, and interstitial integrity. Pathological signs such as germ cell degeneration, vacuolization, multinucleated cells, or disrupted tubule organization were recorded. Images were taken for documentation and compared to age-matched controls.

Intracytoplasmic sperm injection (ICSI) and offspring / fertility analysis

ICSI was performed using testicular sperm from treated males. Mature metaphase II oocytes were obtained from superovulated C57BL/6J females (6–8 weeks) induced with PMSG (NSHF, Cat#110254564) and hCG (NSHF, Cat#A2212051). Cumulus–oocyte complexes were harvested 14 h post-hCG, cumulus cells removed with hyaluronidase (300 µg/mL; Sigma, H4272), and denuded oocytes maintained in KSOM medium (AibeiBio, M1435) under mineral oil (Sigma, M5310-500ML).

Testes from treated males (10–13 days post-injection) were digested with collagenase IV (0.4 mg/mL; Worthington LS004188) and DNase I (10 µg/mL; Roche 10104159001), followed by trypsin-EDTA (0.25%; Gibco 25200072). Digestion was quenched with FBS. Suspensions were filtered, centrifuged, and resuspended in GBSS + 5% FBS + DNase I. Only morphologically normal motile or twitching spermatozoa were selected.

ICSI was performed essentially as described[42,43] using a piezo-electric manipulator (Eppendorf PiezoXpert). Individual sperm were drawn tail-first into injection pipettes (6.5–8.5 µm ID) containing polyvinylpyrrolidone (Vitrolife, 10111). After injection, embryos were cultured to the 2-cell stage (24 h) and transferred into pseudopregnant ICR females (8–10 embryos per oviduct). Litters were delivered naturally. Offspring were monitored for growth, health, endocrine status, fertility, and overall development.

Behavioral assays and sexual activity

Behavioral assays were performed during the light phase after a 1-week habituation.

Open field test[44]: Mice were placed in a 40 × 40 × 40 cm Plexiglass arena for 10 min under 650 lux illumination. Activity was video recorded and analyzed using EthoVision XT. Measures: distance traveled, average speed, and time spent in center vs. periphery. Arenas were cleaned with 70% ethanol between trials.

Novel object recognition test[45]: Day 1: habituation. Day 2: exposure to two identical objects for 10 min. Day 3: one object replaced with a novel one. Recognition index = time with novel / (time novel + time familiar) × 100%.

Object location memory test: Same as NOR, except one object was moved to a new position on Day 3. Location index = time with moved / (time moved + time stationary).

Sexual activity assay[46]: Female mice (≥6 weeks old) were bilaterally ovariectomized under isoflurane anesthesia, given postoperative antibiotics and analgesics, and housed singly until recovery. To induce estrus, females received estradiol benzoate (20 µg in 0.1 mL olive oil, i.p.) 48 h before testing and progesterone (500 µg in 0.1 mL oil, i.p.) 4 h before testing. Estrous status was confirmed by vaginal smears. Sexual behavior tests were conducted in a 40 × 40 × 40 cm Plexiglass open-field arena under dim light at the beginning of the dark cycle. Males were habituated to the apparatus for 2 days. Interactions with primed females were video-recorded for 30 min. Metrics: mounting latency, intromission latency, ejaculation latency, post-ejaculatory interval, copulatory series number and duration, number of mounts and intromissions. Apparatus was cleaned with 75% ethanol after each test. Observers were blinded to groups.

Gene expression (qRT-PCR) & Protein analysis

qRT-PCR: RNA was extracted from flash-frozen testes or other tissues with TRIzol (Thermo Fisher 10296028), DNase treated (Turbo DNase, Thermo AM2239), quantified, and reverse transcribed with HiScript III RT SuperMix (Vazyme R323-01). qPCR was performed on a BIO-RAD CFX-96 with SYBR Green master mix (Vazyme Q712-02). Primers spanned exon–exon junctions (see Supplementary Table 1). *Actb* served as housekeeping control. Reactions were run in triplicate. Relative expression was calculated using the ΔΔCq method with efficiency correction[47]. Specificity was validated by melt curves and gel electrophoresis.

Western blot: Proteins were extracted in NP40 buffer (Sangon Biotech 9016-45-9) with protease inhibitors, quantified by BCA assay, separated by SDS–PAGE, transferred to PVDF membranes (PALL BSP0161), and probed with anti-HA (CST C29F4, 1:1000) and anti-GAPDH (Proteintech 60004-1-Ig, 1:5000). HRP-conjugated secondaries and ECL detection (Thermo 34577) were used. Each experiment included 3 biological replicates.

Hematology and serum biochemistry

Blood was collected via retro-orbital sinus or cardiac puncture. CBCs were measured with Sysmex xn9000. Serum biochemistry (ALT, AST, ALP, bilirubin, BUN, creatinine, electrolytes, glucose) was measured using HITACHI LABOSPECT 008 AS. Analyses were performed blinded to group identity.

Imaging of LNPs by Transmission Electron Microscopy (TEM)

For TEM observation, 5 μL of each LNP sample was applied to a carbon-coated copper grid and allowed to adsorb for ~1 min at room temperature. Excess liquid was then removed with filter paper, followed by negative staining with 2% uranyl acetate for 45–60 s. The grid was blotted dry and air-dried before imaging. TEM images were acquired using a Tecnai G2 Spirit BioTwin transmission electron microscope (FEI, USA) operated at 120 kV. Additionally, for fluorescence microscopy assessment, 5 μL of LNP

dispersion (with fluorescent tracer incorporated) was spotted on a glass slide, air-dried in the dark for ~30 min, and then imaged by epifluorescence microscopy to qualitatively examine LNP fluorescence signals.

Culture and Treatment of Human Seminiferous Tubules

Human seminiferous tubule fragments were obtained from donor testicular tissue under an approved human ethics protocol (No. 20130009 and K2026019) from Zhejiang University huma ethics review board. For organ culture, an agarose gel base was prepared by dissolving 0.05 g of agarose in 5 mL ultrapure water, melting it via microwave, and dispensing the solution into a white 96-well plate; the agarose was allowed to cool and solidify at room temperature, forming a half-volume gel layer at the bottom of each well. This soft agarose layer served as a support to maintain an air–medium interface for the explanted tissue[48–50]. Each well was then overlaid with 100 μL of complete culture medium (Procell, CM-H191). Small fragments of human seminiferous tubules were placed in the medium (on top of the gel) and incubated at 33 °C in a humidified 5% CO_2 atmosphere for 1–2 h to equilibrate. Subsequently, Luci MC3 LNP (containing the codon-optimized luciferase mRNA) was added to the wells (typically in a 1:100–1:500 dilution of the stock into the culture medium), and the samples were further incubated under the same conditions for either 24 h or 48 h. After the incubation period (at the designated 24 h or 48 h endpoint), the medium was removed from each well. Then, 100 μL of a detection working solution – composed of 50 μL culture medium mixed with 50 μL of luciferase substrate reagent (Beyotime, Cat. RG043M) – was added to each well, directly covering the tubule fragments. After a 5 min incubation at room temperature to allow substrate penetration and signal development, bioluminescence from the luciferase-expressing tubule fragments was measured using a Spark multimode microplate reader (Tecan), with an integration time of 0.5 s per well. (Luminescence readings were performed for both 24 h and 48 h treated samples to assess transfection efficacy over time.)

Fluorescence "Squash" Immunostaining

To visualize luciferase expression within the seminiferous tubule cells, a squash immunostaining technique was employed. Cultured human tubule fragments were first fixed in 2% paraformaldehyde (in 1× PBS containing 0.1% Triton X-100) for 5–10 min at room temperature. Each fragment was then gently placed on a glass microscope slide, overlaid with a coverslip, and lightly pressed to flatten the tubule ("squash" preparation). The slide with coverslip was quickly plunged into liquid nitrogen, freezing the sample. Once frozen, the coverslip was pried off, leaving the flattened tubule tissue adhered to the slide. The slides were stored at −80 °C until immunostaining. For staining, slides were brought to room temperature and washed three times with PBS (5 min each). The tissue was then incubated overnight at 4 °C in a humidified chamber with primary antibody against firefly luciferase (rabbit polyclonal, Abcam ab185924, 1:500 dilution in PBS). The next day, slides were washed in PBS three times (10 min each). A secondary antibody (goat anti-rabbit IgG conjugated to Alexa Fluor 488, Invitrogen A11008) diluted 1:500 in PBS was applied to the samples, and slides were incubated for 1–2 h at room temperature in the dark. After secondary incubation, slides were washed again in PBS (3 × 10 min). Finally, samples were mounted with Vectashield antifade medium containing DAPI (Vector Laboratories H-1200) to counterstain nuclei, and a coverslip was applied and sealed with nail polish. Immunofluorescence images were captured using a fluorescence microscope. The resulting images allowed identification of Luci mRNA-translated protein (luciferase) within the tubule cells (green fluorescence), alongside nuclear staining (blue).

TUNEL Assay for Apoptosis Detection in Testis

Apoptotic cells in mouse testes were detected using a one-step TUNEL (TdT-mediated dUTP nick-end labeling) in situ apoptosis detection kit (Elabscience, Cat. E-CK-A321, FITC Green). Whole testes from mice were fixed in 4% paraformaldehyde (pH 7.4) at 4 °C overnight, then cryoprotected by soaking in 30% sucrose, embedded in OCT

compound, and cryosectioned at 5 μm thickness. Frozen sections were equilibrated to room temperature, then post-fixed in 4% PFA for 30 min and washed with PBS (3 × 5 min). Sections were permeabilized with 100 μL of Proteinase K working solution at 37 °C for 20 min, followed by three PBS washes. Next, 100 μL of TdT Equilibration Buffer was applied for 20 min at 37 °C, and subsequently 50 μL of TUNEL reaction mixture (label and enzyme) was added to each section. Slides were incubated in a humidified chamber at 37 °C for 1 h in the dark. For negative-control sections, the TdT enzyme was omitted (to confirm specificity of staining), while for positive controls, sections were pre-treated with DNase I to fragment DNA before TUNEL labeling. After the 1 h incubation, sections were washed with PBS (3 × 5 min), then counterstained with DAPI for 5 min to label nuclei. After four final rinses in PBS, sections were mounted with antifade medium and coverslipped. Fluorescent images of the sections were acquired (TUNEL-positive nuclei appearing as green punctate nuclear fluorescence). Using ImageJ software, the apoptotic index in each section was quantified as described[51]. TUNEL fluorescence intensity (gray value) was measured to indicate the apoptotic signal, while DAPI-stained nuclear area was used to normalize for total cell number. The apoptotic index was calculated as the ratio of TUNEL gray value to total DAPI-positive nuclear area, representing the mean optical density of the TUNEL signal per seminiferous tubule.

Hormone Measurement by ELISA

Serum hormone levels were measured by enzyme-linked immunosorbent assay (ELISA). In particular, testosterone, luteinizing hormone (LH), and follicle-stimulating hormone (FSH) concentrations in culture media (or serum, as applicable) were quantified using commercial ELISA kits: Testosterone ELISA Kit (SIMI BIO, Cat. ME-M1435S), Luteinizing hormone ELISA Kit (SIMI BIO, Cat. ME-M1128), and FSH ELISA Kit (SIMI BIO, Cat. ME-M1539S). All procedures were carried out according to the manufacturers' instructions. At the conclusion of the culture or treatment period, samples

were collected and incubated with the kit's assay reagents in 96-well plate format. Absorbance readings were taken on a microplate spectrophotometer, and hormone concentrations were calculated based on the standard curves provided in the kit manuals. Results were reported in ng/mL for testosterone and mIU/mL for FSH, consistent with kit specifications.

Primers and antibodies

Primer sequences (e.g., *Papolb* forward 5′-CTGTCCATCGACCTGACTTATG-3′; reverse 5′-GCAACTGGTGCAGTTCTTTC-3′; *Actb* forward 5′-TCTAGACTTCGAGCAGGAGATG-3′; reverse 5′-GAACCGCTCGTTGCCAATA-3′) are listed in Supplementary Table 1. Antibody information (host, catalog number, lot, dilution) is also in Supplementary Table 1. Specificity was validated by omission and isotype controls.

Alkaline Comet Assay

Sperm DNA integrity was assessed using a modified alkaline comet assay (C2041M, Beyotime) adapted for protamine-condensed chromatin. Briefly, sperm washed in Ca^{2+}/Mg^{2+}-free PBS were embedded in 0.7% low-melting-point agarose on frosted slides. Positive controls were generated by treating sperm with 100 μM H_2O_2 for 30 min at 4 °C. Lysis was performed in two steps. Slides were first incubated in standard lysis buffer (2.5 M NaCl, 100 mM EDTA, 10 mM Tris, 1% Triton X-100, pH 10) for 1 h at 4 °C. This was followed by enzymatic de-protamination in lysis buffer supplemented with 10 mM DTT and 1 mg/mL Proteinase K for 1.5 h at 37 °C. Slides were then equilibrated in alkaline electrophoresis buffer (300 mM NaOH, 1 mM EDTA, pH >13) for 20 min and electrophoresed at 25 V for 10–20 min. After neutralization, DNA was stained with propidium iodide (PI). Images were captured using a fluorescence microscope (Zeiss Axio Imager.M2)

Masson Trichrome Staining

Masson's trichrome staining (C0189M, Beyotime) was used to assess tissue fibrosis and collagen deposition. Tissue samples were fixed in 4% paraformaldehyde overnight, dehydrated through a graded ethanol series, and embedded in paraffin. Sections (3 μm thickness) were deparaffinized in xylene and rehydrated using standard protocols. Sections were stained with hematoxylin for 5 min, differentiated in acid alcohol, and blued in running tap water. Slides were then stained with Ponceau–acid fuchsin for 10 min to visualize cytoplasm and muscle fibers (red), followed by differentiation with phosphomolybdic acid. Collagen fibers were counterstained with Light Green solution for 1 min and briefly differentiated in acetic acid. Finally, sections were dehydrated in ethanol, cleared in xylene, and mounted with neutral resin. Slides were evaluated by an investigator blinded to experimental groups. Fibrosis was assessed based on collagen deposition and tissue structural integrity.

Diff-Quik Staining

Cellular and histological specimens were stained using a Diff-Quik Stain Kit (40748ES, Beyotime) according to the manufacturer's instructions. For tissue sections, slides were hydrated in distilled water and sequentially immersed in Stain Solution I for 10–20 s and Stain Solution II for 10–20 s with gentle agitation. Slides were rinsed in distilled water and dehydrated twice in absolute ethanol. For smear samples (e.g., sperm smears), slides were air-dried for at least 15 min and fixed in Fixative Solution for 10–20 s. Slides were then stained in Stain Solution I for 5–10 s followed by Stain Solution II for 5–10 s. After rinsing with distilled water and dehydration in ethanol, slides were air-dried, cleared, and mounted for microscopic examination.

Measurement of mitochondrial membrane potential (Δψm) using JC-1

Mitochondrial membrane potential (Δψm) of spermatozoa was assessed using the JC-1 fluorescent probe (C2003, Beyotime). Sperm concentration was adjusted to 1×10^6 cells/mL and incubated with 1× JC-1 working solution at 37 °C for 20 min in the dark.

After staining, cells were washed once with JC-1 staining buffer (500 × g, 5 min), resuspended, and mounted for fluorescence imaging. Green fluorescence (JC-1 monomers, λex/λem ≈ 490/530 nm) and red fluorescence (JC-1 aggregates, λex/λem ≈ 525/590 nm) were captured under identical imaging parameters. Mitochondrial membrane potential was quantified as the ratio of red to green fluorescence intensity. As a positive control for mitochondrial depolarization, samples were pretreated with 10 μM CCCP at 37 °C for 10 min prior to staining.

TMRE staining for mitochondrial membrane potential

To evaluate Δψm of spermatozoa, cells were stained with tetramethylrhodamine ethyl ester (TMRE; HY-D0985A, MCE). Sperm samples were adjusted to 1×10^6 cells/mL and incubated with 50 nM TMRE for 20 min at 37 °C in the dark. After incubation, cells were washed once with PBS, resuspended, and mounted on glass slides for live-cell fluorescence imaging. All images were acquired using identical excitation wavelength, exposure time, and detector gain to ensure comparability between groups.

MitoTracker staining

To visualize mitochondrial architecture in spermatozoa, cells were stained with the potential-dependent fluorescent probe MitoTracker Deep Red FM (M22426, Invitrogen). Sperm samples were adjusted to 1×10^6 cells/mL and incubated with 100 nM MitoTracker Deep Red FM for 30 min at 37 °C in the dark. After staining, cells were washed once with PBS (500 × g, 5 min) and mounted for fluorescence microscopy. Mitochondrial signals were captured using a far-red filter set (λex/λem ≈ 644/665 nm). Fluorescence distribution along the sperm midpiece was used to assess mitochondrial integrity and localization.

Chromosome spread immunostaining

Chromosome spread immunostaining was performed as previously described[52,53]. Briefly, testes were rinsed in cold PBS and the tunica albuginea was removed. Seminiferous tubules were dissociated in DMEM to obtain testicular cell suspensions. Cells were centrifuged at 5800g for 5 min at 4 °C and resuspended in 0.1 M sucrose containing protease inhibitors. Cell suspensions were spread onto slides coated with 1% paraformaldehyde and 0.1% Triton X-100 and incubated overnight in a humid chamber. Slides were washed with PhotoFlo solution and blocked in antibody dilution buffer (ADB). Primary antibodies were applied at 1:500 dilution (mouse anti-SYCP3, ab97672, Abcam; rabbit anti-SYCP1, ab15090, Abcam) and incubated at 37 °C for 2 h. After washing, slides were incubated with Alexa Fluor 488 goat anti-mouse and Alexa Fluor 594 goat anti-rabbit secondary antibodies. Slides were mounted and images were acquired using a Zeiss Axio fluorescence microscope with a 63× oil immersion objective.

Flow cytometry analysis of testicular cells

To quantify in vivo transfection efficiency, single-cell suspensions were prepared from Ai9 mouse testes 48 h after treatment. Decapsulated testes were digested sequentially with collagenase IV (1 mg/mL) and DNase I (0.1 mg/mL) at 33 °C to release interstitial cells, followed by digestion of seminiferous tubules with 0.25% trypsin-EDTA. Cells were filtered through a 70 μm nylon mesh. For germ-cell lineage analysis, cells were stained with Hoechst 33342 (5 μg/mL) for 30 min at 33 °C and propidium iodide (PI) was used to exclude non-viable cells. Data were acquired using a BD LSRFortessa flow cytometer and analyzed with FlowJo software (v10.8). Germ-cell populations were distinguished based on DNA ploidy (1C, 2C, 4C) and cell size (FSC). Transfection efficiency was determined as the percentage of tdTomato-positive cells within each germ-cell population.

Pyrosequencing

Genomic DNA was extracted using DNeasy Blood and Tissue Kits (69504, Qiagen). Bisulfite conversion was performed using the EpiTect Bisulfite Kit (59104, Qiagen). Primers were designed using PyroMark Assay Design 2.0. Target loci were amplified by PCR and sequencing was performed using the PyroMark Q48 platform following the manufacturer's instructions with the condition of 95°C for 3 min, followed by 40 cycles of 94°C for 30 s, 56°C for 30 s, and 72°C for 1 min, and a final extension at 72°C for 7 min. Statistical comparisons for individual CpG sites were corrected for multiple testing using the Benjamini–Hochberg method.

RNA-seq library construction

Total RNA was extracted using the mirVana RNA extraction kit (AM1561, Invitrogen). After DNase treatment (AM2238, Invitrogen), RNA was purified using the RNA Clean & Concentrator-5 Kit (R1013, Zymo Research). Ribosomal RNA was depleted using rDNA probe hybridization followed by RNase H digestion. Strand-specific RNA-seq libraries were prepared using the NEBNext Ultra II Directional RNA Library Prep Kit (E7760S, NEB). Libraries were quantified using Qubit 4.0 and sequenced on a NovaSeq X Plus sequencer (Illumina) with 2 × 150 bp paired-end reads.

Low-input RNA-seq for early embryo transcriptomics

Two-cell and four-cell embryos were rinsed in PBS and flash-frozen in liquid nitrogen. RNA was extracted using TRIzol reagent followed by column purification using the RNA Clean & Concentrator-5 Kit. DNA contamination was removed using DNase treatment. rRNA depletion and library preparation were performed using the Polaris rRNA/Globin Depletion kit (Watchmaker) and Watchmaker RNA Library Prep Kit. For samples containing <1 ng input RNA, additional bead purification steps were performed using DNA Clean Beads (Vazyme) to remove adapter dimers. Libraries were sequenced on the NovaSeq PE150 platform.

Whole-genome sequencing

Genomic DNA was fragmented to 180–280 bp using a Covaris instrument. Libraries were constructed using standard Illumina library preparation procedures, including end repair, adaptor ligation, and PCR amplification. Libraries were quality-checked using an Agilent Bioanalyzer 2100 and sequenced on the Illumina NovaSeq platform.

Bioinformatic analysis

RNA-seq reads were adapter-trimmed using cutadapt[54]. Downstream analyses were performed using piPipes[55]. Transcript abundance was quantified as TPM using the Salmon algorithm[56], and analyzed with DESeq2 (v.1.46.0)[57]. P-values were adjusted for multiple comparisons using the Benjamini–Hochberg procedure. Differential expression was assessed using adjusted $P < 0.05$. DNA-seq reads were trimmed with cutadapt and aligned to the mouse reference genome (mm10) using Bowtie2[58]. Alignments were converted to BAM format and sorted using SAMtools[59]. Genome-wide read-depth profiles were generated using deepTools[60]. Copy-number variation was assessed by calculating $\log_2$ fold changes in read depth using 1 Mb genomic bins. Structural variants were detected using Picard (Broad Institute; https://broadinstitute.github.io/picard/) and Manta[61]. BAM files were aligned to a hybrid reference genome comprising mm10 and the full *Papolb* cDNA sequence.

Statistical analysis

All data are shown as mean ± s.d. unless stated otherwise. GraphPad Prism v9 was used. Two-group comparisons: unpaired two-tailed Student's t-test (if normality passed) or Mann–Whitney U test (if not). Multi-group comparisons: one-way or two-way ANOVA with Tukey's or Bonferroni post hoc correction. Threshold for significance: $P < 0.05$. Significance reported as $P < 0.05$ (*), $P < 0.01$ (**), $P < 0.001$ (***), and $P < 0.0001$ (****). Exact P values provided where possible. Outliers were tested with Grubbs' test ($\alpha = 0.05$). Randomization and blinding were applied where possible. Sample sizes were

determined based on previous studies in the field. No animals were excluded except for technical failures, which did not occur in this study.

Data availability

The RNA-seq and Genome-seq datasets generated in this study have been deposited in the Genome Sequence Archive (GSA) under BioProject accession PRJCA058762 and Sequence Read Archive accession CRA039361. These data will be made publicly available upon publication.

Acknowledgments

We thank Yuchao Sun, Ying Liu, Lejun Zhang, Yuting Wang, Wenying Long, Yao Wu, and Yunpan Wang from the Core Facilities of the Fourth Affiliated Hospital, Zhejiang University School of Medicine, and of the International Institutes of Medicine, Zhejiang University, for their technical support. We are grateful to Beijia Wang, Laijie Ni, Xiangfei Zhang, Yulan Zheng, and Weiwei Jin from the Laboratory Animal Center of the International Institutes of Medicine, Zhejiang University, for their meticulous care of the laboratory mice. We also thank the Pathology Core and the Department of Laboratory Medicine of the Fourth Affiliated Hospital, Zhejiang University School of Medicine, as well as members of the Li laboratory, for assistance and helpful discussions. We thank Chenyu Yang in the Center of Cryo-Electron Microscopy (CCEM), Zhejiang University for her technical assistance on Transmission Electron Microscopy. We acknowledge Levostar and GemPharmatech for their contributions to plasmid construction.

Author Contributions

Qi Kai Jiang and Kexin Su prepared the lipid nanoparticle formulations; Qi Kai Jiang, Yukai Zhong, and Xuliang Ma performed the in vivo mouse experiments; Huali Luo, Qi Kai Jiang, Linlin Zhang, and Haifeng Zhang carried out Immunofluorescence Staining, Masson Staining, Diff Quik Staining and H&E Staining; Jiaoyan Ma performed the

TUNEL staining and mitochondria related experiment; Qi Kai Jiang, Hao Wang, Qiaodan Li, Yukai Zhong, Jingwen Luo, and Xuliang Ma conducted intracytoplasmic sperm injection and embryo transfer; Qi Kai Jiang and Zhihui Zhang performed the complete blood count and serum biochemistry analyses; Jingwen Luo, Qi Kai Jiang, and Xuliang Ma conducted the behavioral tests; Qi Kai Jiang and Banghua He carried out Western blot assays; Qi Kai Jiang, Yukai Zhong, and Qin Li were responsible for photographing and genotyping the "Papi" and other offspring; Guangnan Li, Wenlin Li, and Chenyu Pei performed RNA-seq and DNA-seq library construction, data analysis, and image processing; Deivendran and Qi Kai Jiang performed Chromosome Spreading; X.Z.L. and Qi Kai Jiang analyzed the data; X.Z.L., Qi Kai Jiang and Guangnan Li wrote the paper; X.Z.L., Xianguang Yang, Lejun Li, Shuai Liu, and Zhefan Yuan contributed to the study design. All authors participated in the preparation of the manuscript.

Competing Interests The authors declare no competing interests.

Author Information The authors declare no competing financial interests. Correspondence and requests for materials should be addressed to xinlirna@zju.edu.cn

Reference

1. Chandra, A., Copen, C. E. & Stephen, E. H. Infertility and impaired fecundity in the United States, 1982-2010: data from the National Survey of Family Growth. *Natl Health Stat Report* 1-18, 1 p following 19 (2013).
2. Logan, S., Gu, R., Li, W., Xiao, S. & Anazodo, A. Infertility in China: Culture, society and a need for fertility counselling. *Asian Pacific Journal of Reproduction* **8**, 1-6 (2019).
3. Plaseska-Karanfilska, D. et al. Genetic causes of male infertility. *Balkan J Med Genet* **15**, 31-34 (2012).
4. Jan, S. Z. et al. Unraveling transcriptome dynamics in human spermatogenesis. *Development* **144**, 3659-3673 (2017).
5. Kothandaraman, N., Agarwal, A., Abu-Elmagd, M. & Al-Qahtani, M. H. Pathogenic landscape of idiopathic male infertility: new insight towards its regulatory networks. *NPJ Genom Med* **1**, 16023 (2016).

6. Hu, L. et al. Assisted reproductive technology in China: results generated from data reporting system by CSRM from 2013 to 2016. *Frontiers in Endocrinology* **11**, 458 (2020).
7. Smith, A. D. A. C., Tilling, K., Nelson, S. M. & Lawlor, D. A. Live-Birth Rate Associated With Repeat In Vitro Fertilization Treatment Cycles. *JAMA* **314**, 2654-2662 (2015).
8. Heller, C. G. & Clermont, Y. Spermatogenesis in man: an estimate of its duration. *Science* **140**, 184-186 (1963).
9. Amann, R. P. & Howards, S. S. Daily spermatozoal production and epididymal spermatozoal reserves of the human male. *J Urol* **124**, 211-215 (1980).
10. Townsend, B. A. Human genome editing: how to prevent rogue actors. *BMC Med Ethics* **21**, 95 (2020).
11. Fijak, M., Bhushan, S. & Meinhardt, A. Immunoprivileged sites: the testis. *Methods Mol Biol* **677**, 459-470 (2011).
12. Luaces, J. P., Toro-Urrego, N., Otero-Losada, M. & Capani, F. What do we know about blood-testis barrier? current understanding of its structure and physiology. *Front Cell Dev Biol* **11**, 1114769 (2023).
13. Iguchi, N., Tobias, J. W. & Hecht, N. B. Expression profiling reveals meiotic male germ cell mRNAs that are translationally up- and down-regulated. *Proc Natl Acad Sci U S A* **103**, 7712-7717 (2006).
14. Sun, Y. H. et al. Single-molecule long-read sequencing reveals a conserved intact long RNA profile in sperm. *Nat Commun* **12**, 1361 (2021).
15. Gapp, K. et al. Alterations in sperm long RNA contribute to the epigenetic inheritance of the effects of postnatal trauma. *Mol Psychiatry* (2018).
16. Domazet-Lošo, T. mRNA vaccines: Why is the biology of retroposition ignored. *Genes* **13**, 719 (2022).
17. Du, S. et al. Cholesterol-Amino-Phosphate (CAP) Derived Lipid Nanoparticles for Delivery of Self-Amplifying RNA and Restoration of Spermatogenesis in Infertile Mice. *Adv Sci (Weinh)* **10**, e2300188 (2023).
18. Vilpreux, C. et al. Sperm motility in mice with oligo-astheno-teratozoospermia restored by in vivo injection and electroporation of naked mRNA. *Elife* **13**, (2026).
19. Mashiko, D. et al. Sperm and offspring production in a nonobstructive azoospermia mouse model via testicular mRNA delivery using lipid nanoparticles. *Proc Natl Acad Sci U S A* **122**, e2516573122 (2025).
20. Zhang, C. et al. Testicular mRNA-LNP Delivery: A Novel Therapy for Genetic Spermatogenic Disorders. *Adv Sci (Weinh)* e09855 (2026).
21. Jarzebska, N. T., Mellett, M., Frei, J., Kündig, T. M. & Pascolo, S. Protamine-Based Strategies for RNA Transfection. *Pharmaceutics* **13**, (2021).
22. Yamazaki, Y. et al. In vivo gene transfer to mouse spermatogenic cells by deoxyribonucleic acid injection into seminiferous tubules and subsequent electroporation. *Biol Reprod* **59**, 1439-1444 (1998).
23. Michaelis, M., Sobczak, A. & Weitzel, J. M. In vivo microinjection and electroporation of mouse testis. *J Vis Exp* (2014).

24. Buckley, M. et al. Visualizing lipid nanoparticle trafficking for mRNA vaccine delivery in non-human primates. *Mol Ther* **33**, 1105-1117 (2025).
25. Adams, D. et al. Patisiran, an RNAi Therapeutic, for Hereditary Transthyretin Amyloidosis. *N Engl J Med* **379**, 11-21 (2018).
26. Hedger, M. P. Toll-like receptors and signalling in spermatogenesis and testicular responses to inflammation--a perspective. *J Reprod Immunol* **88**, 130-141 (2011).
27. Li, N., Wang, T. & Han, D. Structural, cellular and molecular aspects of immune privilege in the testis. *Front Immunol* **3**, 152 (2012).
28. Kashiwabara, S. et al. Regulation of spermatogenesis by testis-specific, cytoplasmic poly(A) polymerase TPAP. *Science* **298**, 1999-2002 (2002).
29. Kashiwabara, S. I. et al. PAPOLB/TPAP regulates spermiogenesis independently of chromatoid body-associated factors. *J Reprod Dev* **64**, 25-31 (2018).
30. Kashiwabara, S. I., Tsuruta, S., Okada, K., Yamaoka, Y. & Baba, T. Adenylation by testis-specific cytoplasmic poly(A) polymerase, PAPOLB/TPAP, is essential for spermatogenesis. *J Reprod Dev* **62**, 607-614 (2016).
31. Clermont, Y. & Trott, M. Duration of the cycle of the seminiferous epithelium in the mouse and hamster determined by means of 3H-thymidine and radioautography. *Fertil Steril* **20**, 805-817 (1969).
32. O'Donnell, L., Nicholls, P. K., O'Bryan, M. K., McLachlan, R. I. & Stanton, P. G. Spermiation: The process of sperm release. *Spermatogenesis* **1**, 14-35 (2011).
33. Ko, E. Y., Siddiqi, K., Brannigan, R. E. & Sabanegh, E. S. Empirical medical therapy for idiopathic male infertility: a survey of the American Urological Association. *J Urol* **187**, 973-978 (2012).
34. Baudat, F., Manova, K., Yuen, J. P., Jasin, M. & Keeney, S. Chromosome synapsis defects and sexually dimorphic meiotic progression in mice lacking Spo11. *Mol Cell* **6**, 989-998 (2000).
35. Romanienko, P. J. & Camerini-Otero, R. D. The mouse Spo11 gene is required for meiotic chromosome synapsis. *Mol Cell* **6**, 975-987 (2000).
36. Zhou, L. et al. BTBD18 Regulates a Subset of piRNA-Generating Loci through Transcription Elongation in Mice. *Dev Cell* **40**, 453-466.e5 (2017).
37. Griswold, M. D. Spermatogenesis: The Commitment to Meiosis. *Physiol Rev* **96**, 1-17 (2016).
38. Maier, M. A. et al. Biodegradable lipids enabling rapidly eliminated lipid nanoparticles for systemic delivery of RNAi therapeutics. *Mol Ther* **21**, 1570-1578 (2013).
39. Hassett, K. J. et al. Optimization of Lipid Nanoparticles for Intramuscular Administration of mRNA Vaccines. *Mol Ther Nucleic Acids* **15**, 1-11 (2019).
40. Su, K. et al. Reformulating lipid nanoparticles for organ-targeted mRNA accumulation and translation. *Nat Commun* **15**, 5659 (2024).
41. Mizuno-Iijima, S. et al. Mouse resources at the RIKEN BioResource Research Center and the National BioResource Project core facility in Japan. *Mamm Genome* **33**, 181-191 (2022).

42. Yoshida, N. & Perry, A. C. Piezo-actuated mouse intracytoplasmic sperm injection (ICSI). *Nat Protoc* **2**, 296-304 (2007).
43. Tang, J. et al. Monitoring Blood Glucose in Mouse Offspring after Intracytoplasmic sperm injection - Embryo Transfer. *J Vis Exp* (2024).
44. Gould, T. D. *Mood and Anxiety Related Phenotypes in Mice* (Humana Press, 2016).
45. Leger, M. et al. Object recognition test in mice. *Nat Protoc* **8**, 2531-2537 (2013).
46. Liu, Z. W. et al. Assessment of Sexual Behavior of Male Mice. *J Vis Exp* (2020).
47. Peirson, S. N., Butler, J. N. & Foster, R. G. Experimental validation of novel and conventional approaches to quantitative real-time PCR data analysis. *Nucleic Acids Res* **31**, e73 (2003).
48. Gholami, K., Pourmand, G., Koruji, M., Ashouri, S. & Abbasi, M. Organ culture of seminiferous tubules using a modified soft agar culture system. *Stem Cell Res Ther* **9**, 249 (2018).
49. Song, K. et al. Targeting APLN/APJ restores blood-testis barrier and improves spermatogenesis in murine and human diabetic models. *Nat Commun* **13**, 7335 (2022).
50. Li, C. et al. Lovastatin promotes the self-renewal of murine and primate spermatogonial stem cells. *Stem Cell Reports* **18**, 969-984 (2023).
51. de Noiron, J., Hoareau, M., Colin, J. & Guénal, I. Apoptosis Quantification in Tissue: Development of a Semi-Automatic Protocol and Assessment of Critical Steps of Image Processing. *Biomolecules* **11**, (2021).
52. Li, X. C. & Schimenti, J. C. Mouse pachytene checkpoint 2 (trip13) is required for completing meiotic recombination but not synapsis. *PLoS Genet* **3**, e130 (2007).
53. Li, X. C., Bolcun-Filas, E. & Schimenti, J. C. Genetic evidence that synaptonemal complex axial elements govern recombination pathway choice in mice. *Genetics* **189**, 71-82 (2011).
54. Kechin, A., Boyarskikh, U., Kel, A. & Filipenko, M. cutPrimers: A New Tool for Accurate Cutting of Primers from Reads of Targeted Next Generation Sequencing. *J Comput Biol* **24**, 1138-1143 (2017).
55. Han, B. W., Wang, W., Zamore, P. D. & Weng, Z. piPipes: a set of pipelines for piRNA and transposon analysis via small RNA-seq, RNA-seq, degradome- and CAGE-seq, ChIP-seq and genomic DNA sequencing. *Bioinformatics* **31**, 593-595 (2015).
56. Patro, R., Duggal, G., Love, M. I., Irizarry, R. A. & Kingsford, C. Salmon provides fast and bias-aware quantification of transcript expression. *Nat Methods* **14**, 417-419 (2017).
57. Love, M. I., Huber, W. & Anders, S. Moderated estimation of fold change and dispersion for RNA-seq data with DESeq2. *Genome Biol* **15**, 550 (2014).
58. Langmead, B. & Salzberg, S. L. Fast gapped-read alignment with Bowtie 2. *Nat Methods* **9**, 357-359 (2012).
59. Danecek, P. et al. Twelve years of SAMtools and BCFtools. *Gigascience* **10**, (2021).

60. Ramírez, F. et al. deepTools2: a next generation web server for deep-sequencing data analysis. *Nucleic Acids Res* **44**, W160-5 (2016).
61. Chen, X. et al. Manta: rapid detection of structural variants and indels for germline and cancer sequencing applications. *Bioinformatics* **32**, 1220-1222 (2016).

Figure Legends

Figure 1. Efficient intratubular mRNA delivery and context-dependent biodistribution and inflammation

(a) Bioluminescence imaging comparing luciferase expression after two injection routes in the *same mouse*. The "E" testis received an efferent-duct infusion to access the rete testis and fill seminiferous tubules (intratubular delivery), and the "I" testis received a direct interstitial injection. Quantification is photon flux (mean ± s.d.; n = 3 mice per group). Statistical analysis: two-way ANOVA with Sidak's multiple comparisons test (two-sided).

(b) In vivo bioluminescence time course showing testicular luciferase signal after intratubular injection of luciferase mRNA formulated in MC3, ALC-0315, or SM-102 LNPs. Representative images at 1 h and 24 h are shown. Quantification is photon flux (mean ± s.d.; n = 3 mice per group). Statistical analysis: two-way ANOVA with Sidak's multiple comparisons test (two-sided).

(c) Innate immune response in the testis 12 h after intratubular delivery of luciferase mRNA using different LNP formulations. RT–qPCR measurements of *Il-10*, *Il-12b*, *Tnf-α*, *Cxcl10*, *Il-6*, *Ifnb1*, and *Il-1β*. Untreated control testes (black), MC3 (purple), ALC-0315 (gold), SM-102 (green), and LPS positive control (black; intraperitoneal injection). Data are mean ± s.d. (n = 3 mice per group). Statistical analysis: one-way ANOVA with Tukey's multiple comparisons test. LPS, lipopolysaccharide.

(d) Representative H&E-stained testis sections 12 h after intratubular injection of 10 μg luciferase mRNA LNPs. SM-102–treated testes show interstitial edema and leukocyte

infiltration; MC3- and ALC-0315–treated testes show no evident inflammatory infiltrate. Scale bar, 100 µm. (n = 3 mice/testes per group; representative of 3 sections per testis).

(e) Top: Flow cytometry gating strategy to resolve germ-cell populations based on DNA content and size: pre-leptotene spermatogonia (2N, P5), leptotene/zygotene spermatocytes (S-phase, P6), pachytene spermatocytes (4N, P7), diplotene spermatocytes (4N, P8), secondary spermatocytes (2N, P9), and round spermatids (1N, P10). Bottom: Percentage of tdTomato-positive cells within each gated population 48 h after intratubular delivery of Cre mRNA LNPs formulated with ALC-0315, MC3, or SM-102. Data are mean ± s.d. (n = 6 testes per group). Statistical analysis: one-way ANOVA with Tukey's multiple comparisons test.

(f) Cell-type distribution of LNP transfection in Ai9 reporter testes. Ai9 mice received 8 µg Cre mRNA formulated in ALC-0315, MC3, or SM-102 LNPs. tdTomato (red) reports Cre-mediated recombination; DDX4 marks germ cells (green); nuclei stained with DAPI (blue). Scale bar, 40 µm. Representative images shown (n = 3 mice per group; 3 sections per testis).

Jiang et al, Fig. 1

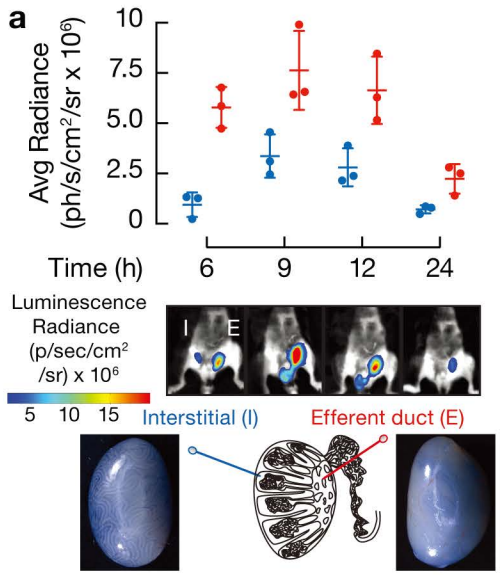

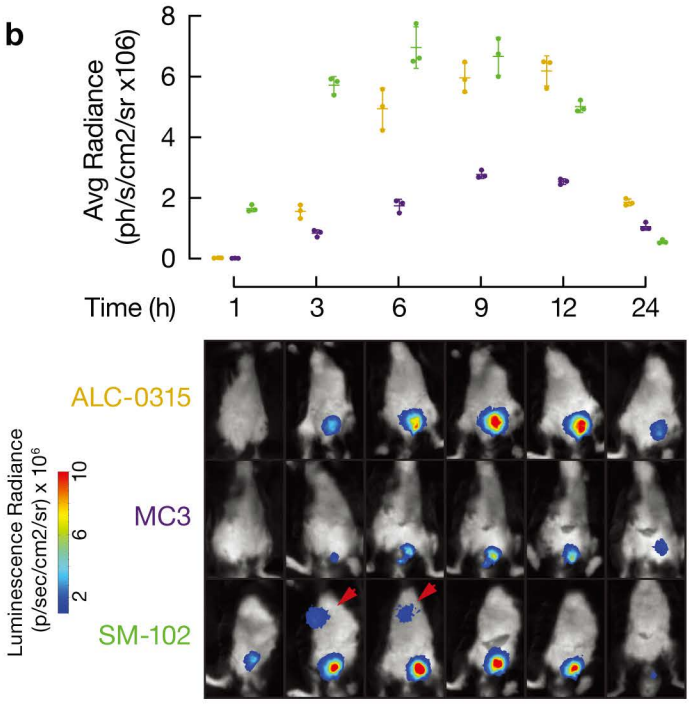

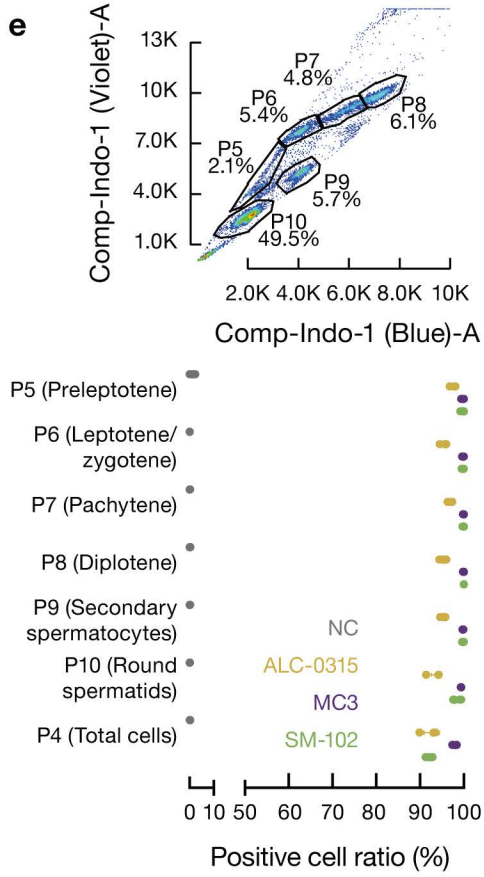

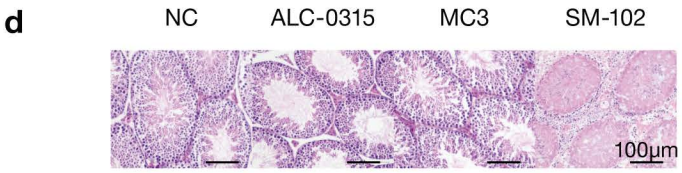

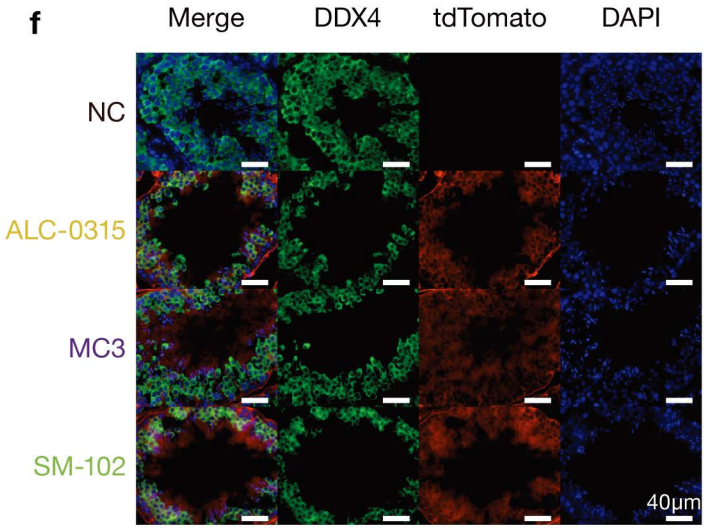

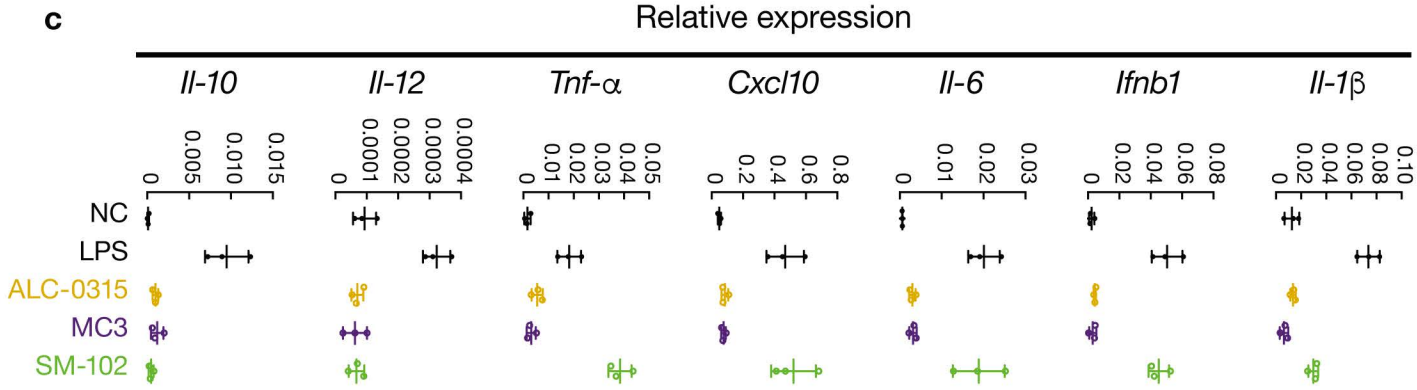

Figure 2. Optimized *Papolb* mRNA formulation sustains expression in testis via MC3 LNP

(a) Schematic of *Papolb* mRNA design: codon-optimized ORF with native 5′UTR and stabilizing human α-globin 3′UTR; HA tag for detection. BTB, blood–testis barrier.
(b) Immunofluorescence detection of HA–PAPOLB (green) in wild-type testis 10 h after intratubular injection of MC3 LNP–*Papolb* mRNA. Scale bar, 40 µm. Representative image shown (n = 3 mice; 3 sections per testis).
(c) Western blot time course of HA–PAPOLB expression following intratubular injection of 10 µg HA–*Papolb* mRNA formulated in MC3 (top) or ALC-0315 (bottom). NC indicates uninjected contralateral testis. GAPDH serves as loading control.
(d) RT–qPCR time course of *Papolb* mRNA persistence in testes following delivery by MC3 vs ALC-0315. Data are mean ± s.d. (n = 3 mice per group per time point). Statistical analysis: two-way ANOVA with Sidak's multiple comparisons test.

Jiang et al, Fig. 2

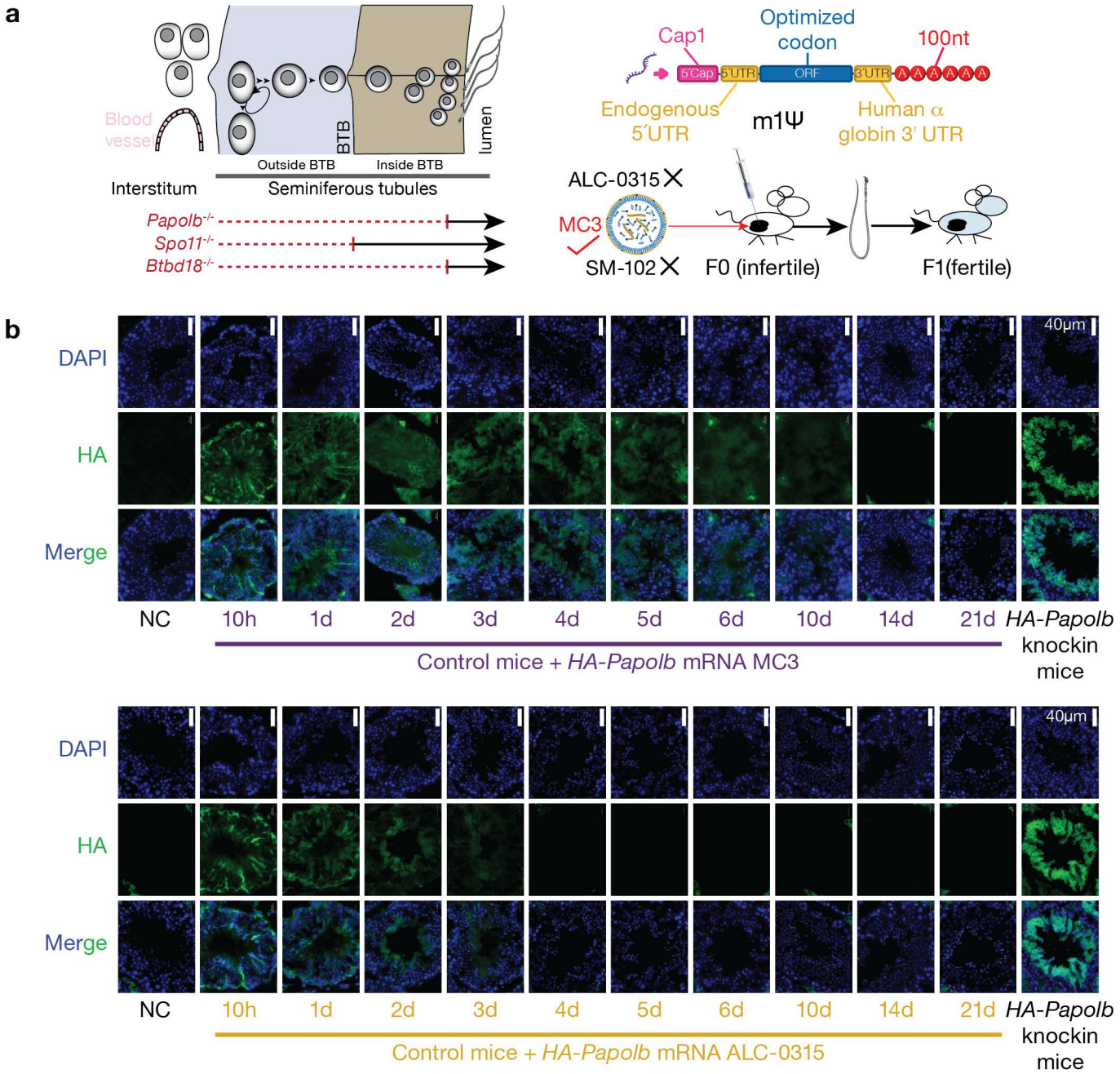

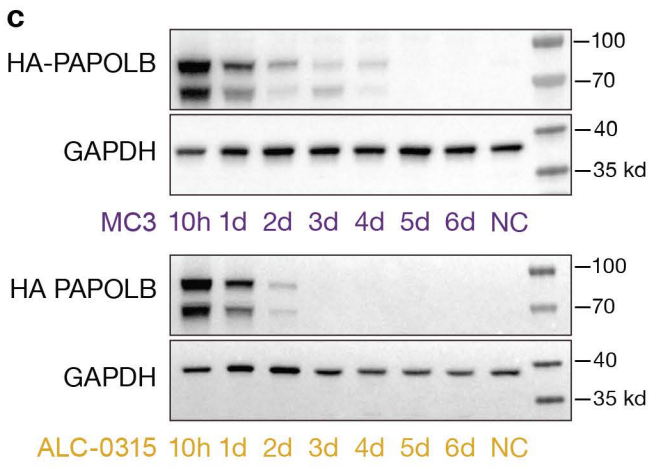

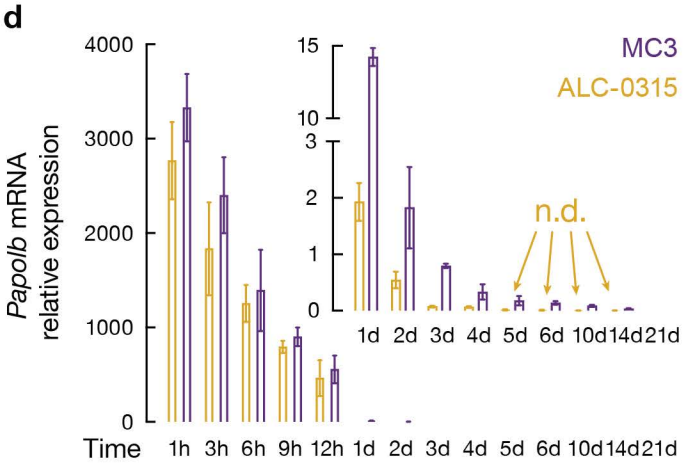

Figure 3. Restoration and transient timeline of spermatogenesis after MC3 LNP–mRNA therapy

(a) H&E-stained seminiferous tubule cross-sections from *Papolb*$^{-/-}$ mutant and *Papolb*$^{+/-}$ heterozygous control mice at day 7 post-treatment. Scale bar, 40 µm. (n = 3 mice per group; representative of 3 sections per testis).
(b) Immunofluorescence staining at day 7 post-treatment showing Protamine-1 (red), PNA acrosome staining (green), and nuclei (DAPI, blue) in *Papolb*$^{-/-}$ testes. Scale bar, 40 µm. (n = 3 mice per group; representative of 3 sections per testis).
(c) H&E-stained testis sections across dose groups compared with untreated *Papolb*$^{+/-}$ controls. Scale bar, 40 µm. (n = 3 mice per dose).
(d) Quantification across dose groups and heterozygous controls: testis mass, percentage of tubules with elongated spermatids, Johnsen score, seminiferous epithelial height, and apoptotic index quantified by TUNEL staining (ratio of TUNEL gray value to total DAPI-positive nuclear area). Data are mean ± s.d. (n = 3 mice per group). Statistical analysis: one-way ANOVA with Tukey's multiple comparisons test. TUNEL, terminal deoxynucleotidyl transferase dUTP nick end labeling
(e) Left, experimental timeline. Right, H&E-stained testis sections from *Papolb*$^{-/-}$ mice at indicated days after a single 8 µg MC3–*Papolb* mRNA injection. Scale bar, 40 µm. (n = 3 mice per time point).

Jiang et al, Fig. 3

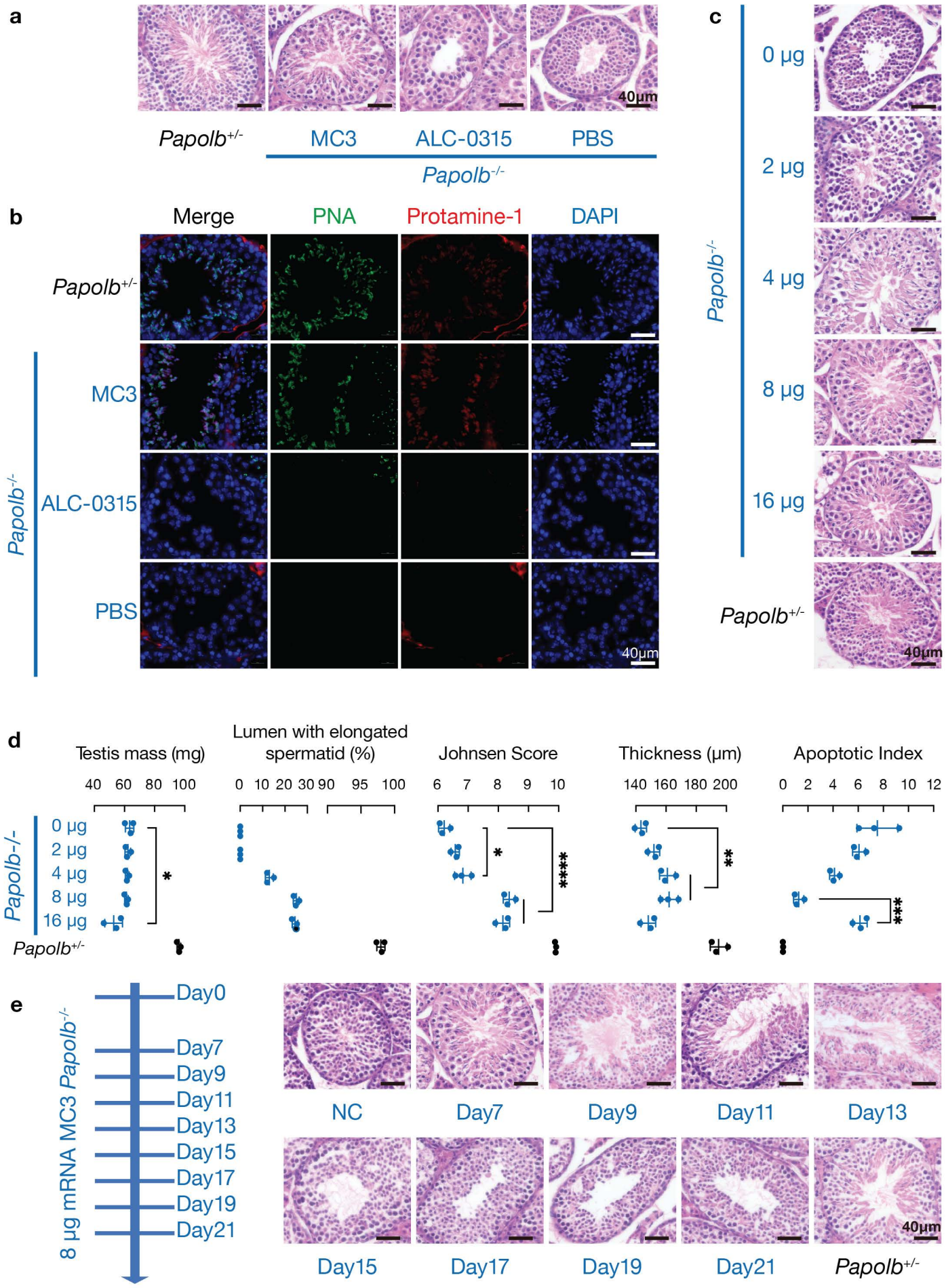

Figure 4. Rescued *Papolb* sperm support embryo development and germline transmission

(a) Bright-field images of sperm isolated from testes ~10–12 days post-treatment. Left: epididymal sperm; middle: testicular sperm from *Papolb*$^{+/-}$ control; right: testicular sperm from MC3-treated *Papolb*$^{-/-}$ male. Scale bar, 10 µm. (n = 3 mice).
(b) Sperm morphology assessed by Diff-Quik staining comparing testicular sperm from treated *Papolb*$^{-/-}$ mice and *Papolb*$^{+/-}$ controls. Scale bar, 10 µm. (n = 3 mice per group; ≥100 sperm scored per mouse).
(c) Mitochondrial membrane potential assessed by JC-1 staining; CCCP-treated sperm served as depolarization control. Scale bar, 10 µm. Quantification shown as red/green ratio (mean ± s.d.; n = 3 mice per group; 200 sperm per mouse). CCCP, carbonyl cyanide m-chlorophenyl hydrazone.
(d) DNA integrity assessed by alkaline comet assay; H_2O_2-treated sperm served as positive control. Scale bar, 20 µm. Quantification shown as tail moment (or % tail DNA) (mean ± s.d.; n = 3 mice per group; 100 sperm per mouse).
(e) Representative two-cell embryos 24 h after ICSI using different sperm sources. Scale bar, 80 µm.
(f) Left, two-cell embryo formation rate (percentage of injected metaphase II oocytes developing to two-cell embryos). Right, live birth rate (percentage of transferred embryos resulting in pups). Data represent mean ± s.d. from four independent experiments (n = 4 ICSI sessions). Statistical analysis: one-way ANOVA with Tukey's multiple comparisons test.
(g) Growth curves (days 7–42) for male and female offspring generated via ICSI (F1) and via natural mating (F2). Data are mean ± s.d. (n = 5 per sex per group). Statistical analysis: two-way ANOVA with Tukey's multiple comparisons test.
(h) Representative locomotor tracks from open-field testing (n = 5 mice per group).
(i) Pups per litter for F1 offspring derived from treated *Papolb*$^{-/-}$ sires versus *Papolb*$^{+/-}$ controls. Data are mean ± s.d. (n = 7 litters per group). Statistical analysis: unpaired t-test

(two-sided).

(j) Serum reproductive hormone levels in treated F0 mice. Testosterone, FSH, and LH were measured by ELISA in *Papolb*$^{+/-}$ controls, untreated *Papolb*$^{-/-}$ (NC), and treated *Papolb*$^{-/-}$ mice at 11 days and 6 months post-treatment. Samples were collected at 9:00–10:00 am. Data are mean ± s.d. (n = 5 mice per group). Statistical analysis: one-way ANOVA with Tukey's multiple comparisons test. FSH, follicle-stimulating hormone; LH, luteinizing hormone.

Jiang et al, Fig. 4

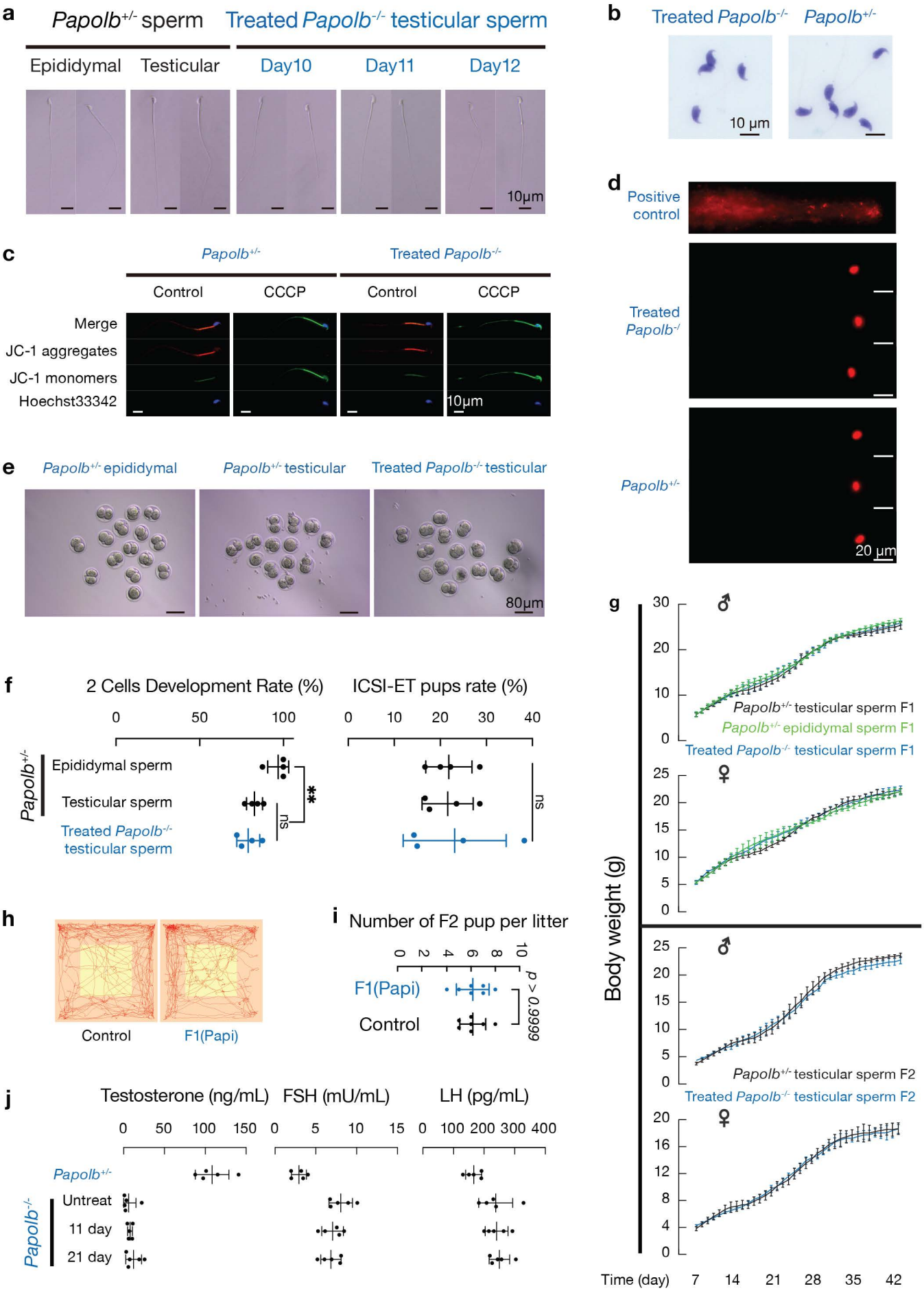

Figure 5. Long-term safety in treated F0 males

(a) F4/80 immunofluorescence analysis of macrophage infiltration in testes at 11 days and 6 months post-treatment. Spleen served as positive control. Scale bar, 50 µm. (n = 3 mice per group; representative of 3 sections per testis).

(b) Masson's trichrome staining of testes at 6 months post-treatment. Skin served as positive control for collagen staining. (n = 3 mice per group; representative of 3 sections per testis).

(c) Claudin11 immunostaining of blood–testis barrier integrity in testes at 11 days and 6 months post-treatment. Scale bar, 50 µm. (n = 3 mice per group; representative of 3 sections per testis).

(d) CYP17A1 immunofluorescence staining in testes of treated and control mice. Scale bar, 50 µm. (n = 3 mice per group).

(e) Western blot of CYP17A1 with densitometric quantification normalized to GAPDH. Data are mean ± s.d. (n = 3 biological replicates). Statistical analysis: one-way ANOVA with Tukey's multiple comparisons test.

(f) Systemic safety evaluation by complete blood count and serum biochemistry. Parameters shown include WBC, platelet count, ALT, AST, BUN, creatinine, and LDH. Data are mean ± s.d. (n = 5 mice per group per time point). Statistical analysis: two-way ANOVA with Tukey's multiple comparisons test. WBC, white blood cell count; ALT, alanine aminotransferase; AST, aspartate aminotransferase; BUN, blood urea nitrogen; LDH, lactate dehydrogenase.

Jiang et al, Fig. 5

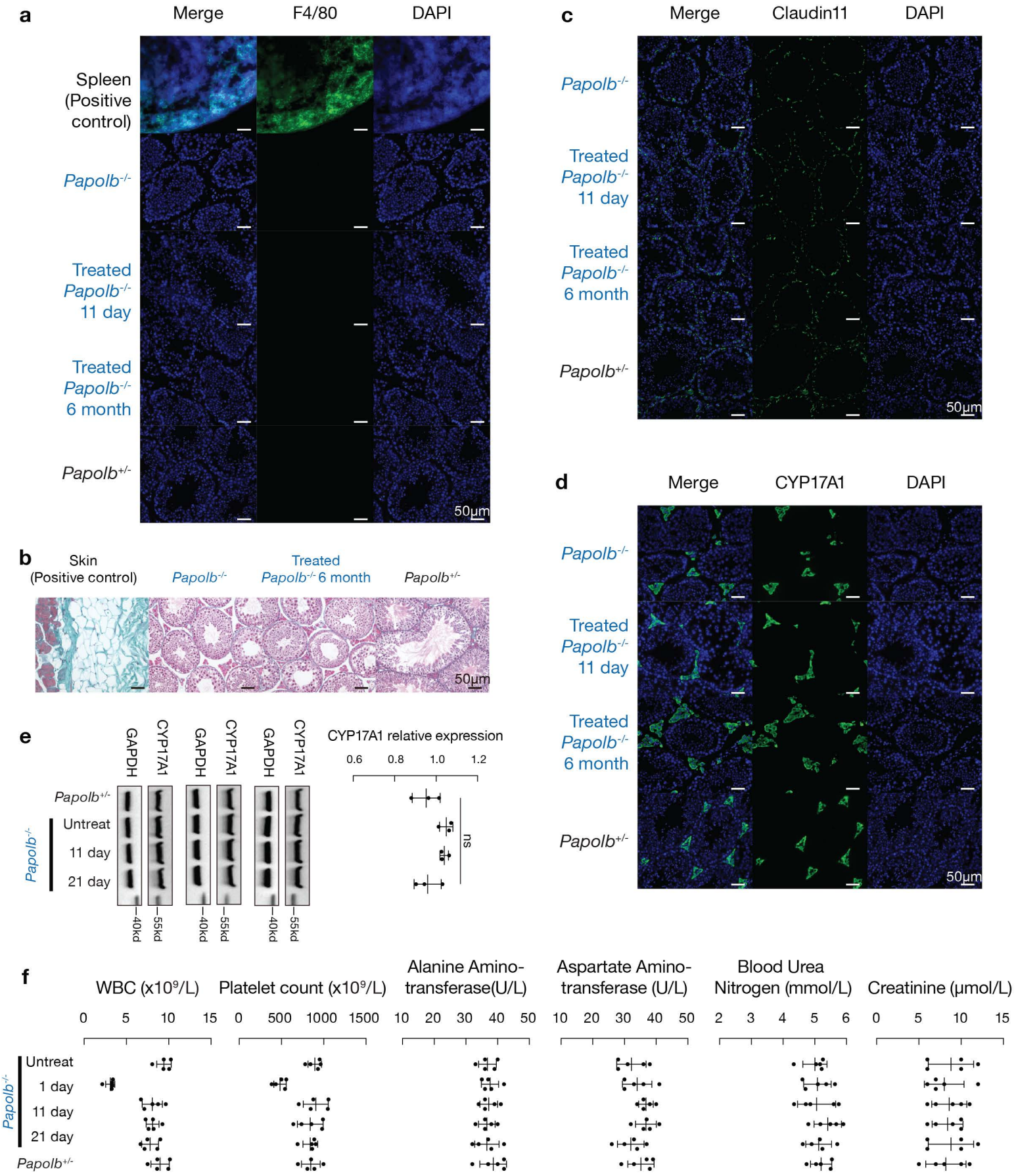

Figure 6. Multigenerational genetic and epigenetic integrity following *Papolb* rescue

(a) DNA methylation at imprinting DMRs (Peg3, Snrpn, H19) measured by pyrosequencing. Dots represent CpG sites; horizontal lines indicate mean methylation. Liver DNA was analyzed. Data are mean ± s.d. (Het = 3; Papi = 4). P-values for individual CpGs were adjusted using Benjamini–Hochberg correction; no CpG remained significant after correction. DMRs, differentially methylated regions; CpG, cytosine-phosphate-guanine.

(b) RNA-seq analysis of early embryos (n = 2 biological replicates per group) and adult tissues (n = 3 biological replicates per group) from Papi and *Papolb*$^{+/-}$ controls. Two-cell and four-cell embryos and adult organs (heart and kidney) were profiled. Differential expression analysis was performed using DESeq2; thresholds: FDR < 0.05 (genes highlighted in blue). Tpm, transcripts per million.

(c) Whole-genome sequencing–based integration analysis. Structural variant detection was performed on reads aligned to a hybrid reference genome containing the mouse genome and the Papolb cDNA contig; no junction-supporting breakend events were detected. n = 3 per tissue group; mean coverage ~30×. CNV analysis is shown in Supplementary Fig. 6c.

(d) PCR sensitivity analysis using serial dilutions of *Papolb* cDNA to establish detection limits for primer sets targeting *Papolb* mRNA; genomic DNA from offspring showed no amplification consistent with integration. (n = 3).

Jiang et al, Fig. 6

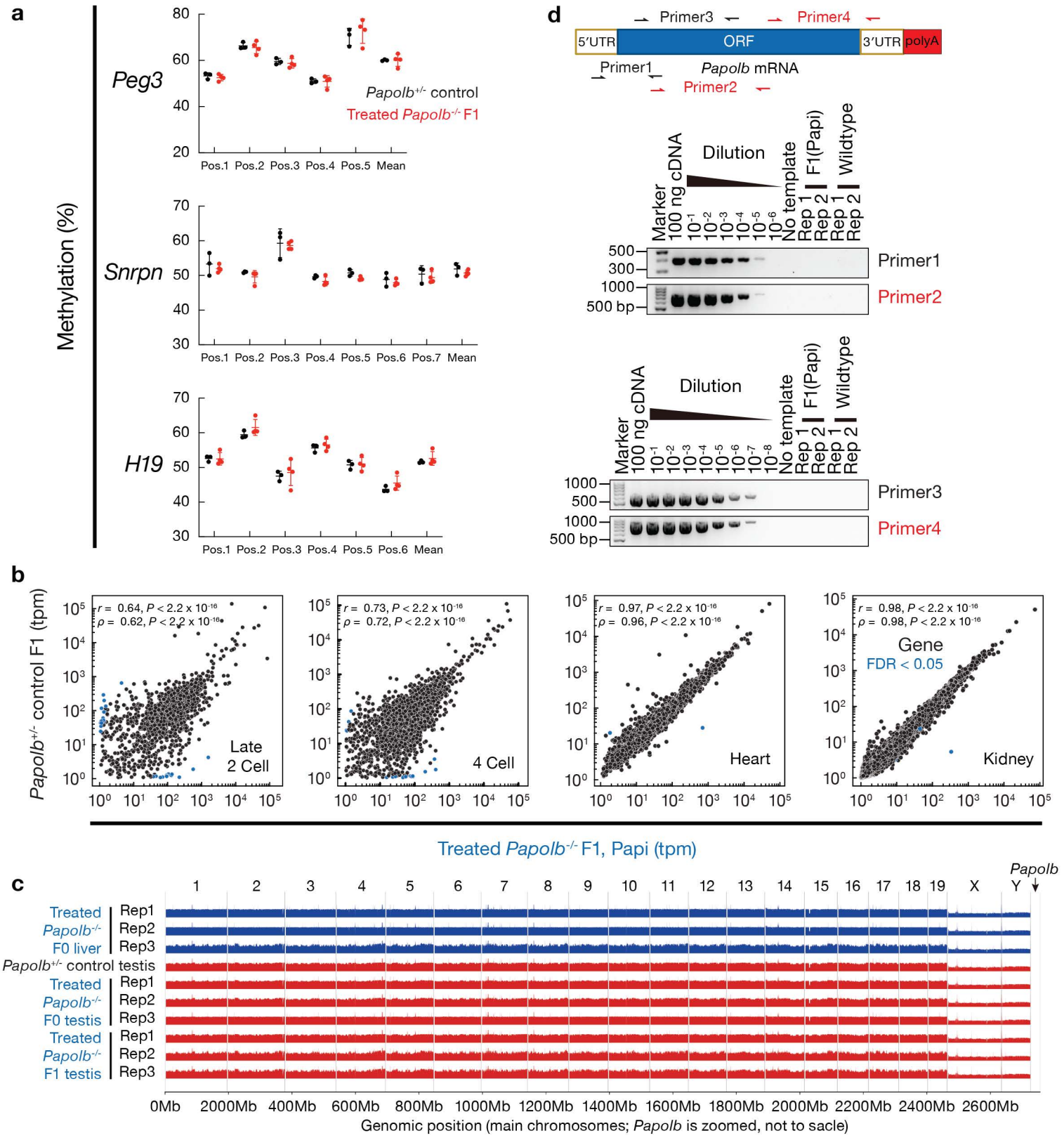

Figure 7. Extension to additional infertility models and human seminiferous tubules

(a) Chromosome spread analysis of *Spo11* rescue. SYCP3 (green) and SYCP1 (red) staining. *Spo11*$^{-/-}$ cells arrest at early zygotene; treated *Spo11*$^{-/-}$ testes show pachytene and diplotene cells. Scale bar, 20 µm. (n = 3 mice per group; 100 nuclei scored per mouse).

(b) H&E staining showing emergence of elongating spermatids at indicated days post-treatment in *Spo11*$^{-/-}$ and *Btbd18*$^{-/-}$ testes. Scale bar, 40 µm. (n = 3 mice per group per time point).

(c) Quantification of rescued tubules (PNA-positive) at peak time points for *Spo11* and *Btbd18* rescue. Tubules counted as 100 tubules per section × 3 sections per testis (n = 3 mice per group). Statistical analysis: one-way ANOVA with Tukey's multiple comparisons test.

(d) Two-cell embryo formation after ICSI using testicular sperm from treated *Spo11*$^{-/-}$ or *Btbd18*$^{-/-}$ males compared with heterozygous controls. Scale bar, 80 µm. (n = 4 sessions; ~20 embryos per group per session). Statistical analysis: unpaired t-test (two-sided).

(e) Postnatal growth curves for male and female F1 offspring derived by ICSI using sperm from treated *Spo11*$^{-/-}$ or *Btbd18*$^{-/-}$ males compared with heterozygous controls. Data are mean ± s.d. (n = 5 per sex per group). Statistical analysis: two-way ANOVA with Tukey's multiple comparisons test.

(f) Luciferase activity in cultured human seminiferous tubules at 0, 24, and 48 h after LNP exposure. (n = 2 donors; 3 replicates per donor). Statistical analysis: one-way ANOVA with Tukey's multiple comparisons test.

(g) HA and RNF17 co-localization in human tubule cultures. Scale bar, 20 µm (main) and 3 µm (zoom). (n = 3 donors).
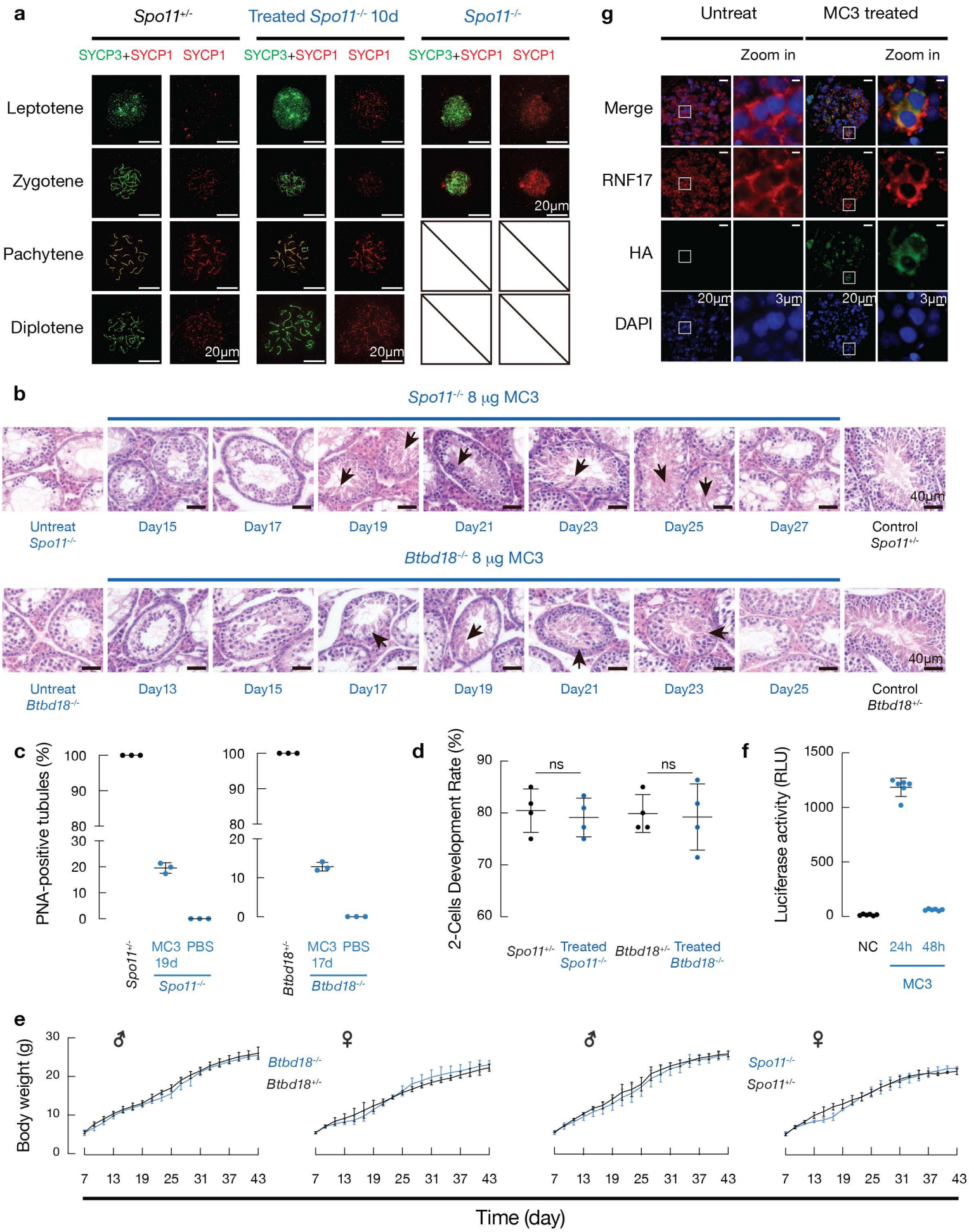
Jiang et al, Fig. 7